J. Fluid Mech. (2014), *vol.* 741, *pp* 461–491.
doi:10.1017/jfm.2013.673

Solutal-convection regimes in a two-dimensional porous medium

Anja C. Slim†

Schlumberger–Doll Research, 1 Hampshire Street, Cambridge, MA 02139, USA

(Received 28 December 2012; revised 8 August 2013; accepted 18 December 2013;
first published online 17 February 2014)

We numerically characterize the temporal regimes for solutal convection from almost first contact to high dissolved solute concentration in a two-dimensional ideal porous layer for Rayleigh numbers $\mathscr{R}$ between 100 and 5×10^4. The lower boundary is impenetrable. The upper boundary is saturated with dissolved solute and either impermeable or partially permeable to fluid flow. In the impermeable case, initially there is pure diffusion of solute away from the upper boundary, followed by the birth and growth of convective fingers. Eventually fingers interact and merge, generating complex downwelling plumes. Once the inter-plume spacing is sufficient, small protoplumes reinitiate on the boundary layer and are swept into the primary plumes. The flow is now in a universal regime characterized by a constant (dimensionless) dissolution flux $F = 0.017$ (the rate at which solute dissolves from the upper boundary). The horizontally averaged concentration profile stretches as a simple self-similar wedge beneath a diffusive horizontal boundary layer. Throughout, the plume width broadens proportionally to $\sqrt{t}$, where t is (dimensionless) time. The above behaviour is parameter independent; the Rayleigh number only controls when transition occurs to a final $\mathscr{R}$-dependent shut-down regime. For the constant-flux and shut-down regimes, we rigourously derive upscaled equations connecting the horizontally averaged concentration, vertical advective flux and plume widths. These are partially complete; a universal expression for the plume width remains elusive. We complement these governing equations with phenomenological boundary conditions based on a marginally stable diffusive boundary layer at the top and zero advective flux at the bottom. Making appropriate approximations in each regime, we find good agreement between predictions from this model and simulated results for both solutal and thermal convection. In the partially permeable upper boundary case, fluid from the convecting layer can penetrate an overlying separate-phase-solute bearing layer where it immediately saturates. The regime diagram remains almost the same as for the impermeable case, but the dissolution flux is significantly augmented. Our work is motivated by dissolution of carbon dioxide relevant to geological storage, and we conclude with a simple flux parameterization for inclusion in gravity current models and suggest that the upscaled equations could lay the foundation for accurate inclusion of dissolution in reservoir simulators.

Key words: convection, convection in porous media

†Email address for correspondence: anja.slim@gmail.com

1. Introduction

Convection in porous media is an important process in many geological and industrial settings (Nield & Bejan 2006). It has recently received renewed attention because of its potential role (Weir, White & Kissling 1996; Lindeberg & Wessel-Berg 1997) in geological carbon-dioxide (CO_2) storage, a short-term implementable technology for reducing anthropogenic CO_2 emissions to the atmosphere (Metz *et al.* 2005). The idea is to sequester CO_2 in porous, brine-filled formations at 1–3 km depth. There the CO_2 is positively buoyant and rises until it encounters a cap rock, beneath which it spreads primarily horizontally. The separate-phase CO_2 gradually dissolves into the underlying brine. Initially this occurs by diffusion, however CO_2-enriched brine is denser than pure brine and the layer may eventually become gravitationally unstable and experience convective overturning. Understanding the dissolution process is of practical interest, because it improves storage security by changing the relative buoyancy of the CO_2.

Here we numerically study two-dimensional solutal convection from a noisy initial condition in a simple, idealized geometry. This geometry consists of a horizontal porous layer with an impenetrable lower boundary and a solute-saturated upper boundary that is either impermeable or partially permeable to flow. The latter mimics the scenario (relevant to CO_2 storage) where solute only partially occupies the pore space above the actively convecting layer. We present the full dynamical picture from almost first contact between solute and solvent through to high dissolved solute saturation for Rayleigh numbers $\mathscr{R}$ (the dimensionless layer thickness and the only parameter) between 100 (just above the stability boundary) and 5×10^4 (well into the 'chaotic' regime). Our objectives are:

(a) a further characterization of key dynamical regimes;
(b) a universal dissolution-flux parameterization; and
(c) universal and physically substantiated upscaled equations.

Solutal convection differs fundamentally from the thermal convection problem that is more conventionally studied, in which impermeable boundaries have a prescribed temperature, because the transient behaviour is of interest rather than the final, statistically steady state. In the thermal case, regime changes occur with increasing Rayleigh number (in this context usually interpreted as the ratio of diffusive to convective time scales across the layer). For $\mathscr{R} < 4\pi^2$ there is pure conduction (Horton & Rogers 1945; Lapwood 1948), while for $4\pi^2 < \mathscr{R} \lesssim 500$ there are steady rolls (Busse & Joseph 1972; Fowler 1997) and for $500 \lesssim \mathscr{R} \lesssim 1300$ there are perturbed rolls (Graham & Steen 1994). Finally, for $\mathscr{R} \gtrsim 1300$ there is a chaotic regime with vertical columnar exchange flow in the bulk and horizontal boundary layers at the upper and lower surfaces on which 'protoplumes' form (Otero *et al.* 2004; Hewitt, Neufeld & Lister 2012).

In solutal convection, regime changes occur in time rather than with Rayleigh number (Slim *et al.* 2013). The dynamics are initially localized to the source of solute at the upper boundary and the layer thickness does not play a role until plumes reach the bottom boundary. Thus, most regimes are parameter independent and the Rayleigh number only controls how many of these regimes are encountered before the bottom influences the dynamics and the flow transitions to a final $\mathscr{R}$-dependent regime. For a flow-impermeable upper boundary, there are a number of studies based on simulations (for example Riaz *et al.* 2006; Hassanzadeh, Pooladi-Darvish & Keith 2007; Rapaka *et al.* 2008; Pau *et al.* 2010; Xie, Simmons & Werner 2011; Elenius & Johannsen 2012; Hidalgo *et al.* 2012; Hewitt, Neufeld & Lister 2013) and experiments (Elder

1968; Neufeld *et al.* 2010; Backhaus, Turitsyn & Ecke 2011; Kneafsey & Pruess 2011; Slim *et al.* 2013). We summarize the rich dynamics these studies unveil into the regime decomposition proposed by Slim *et al.* (2013) for $\mathscr{R} \lesssim 2000$ (note that for the first three regimes Elder 1968, gave a more refined decomposition).

(a) Initially there is a *diffusive regime* in which perturbations decay and the solute profile tends to the standard, purely diffusive error function. The dissolution flux decays proportionally to $\hat{t}^{-1/2}$, where $\hat{t}$ is time.

(b) Eventually, sufficient dense fluid accumulates beneath the upper boundary for perturbations to amplify in a *linear-growth regime*. Various theoretical estimates exist for when onset occurs (see, for example, Ennis-King, Preston & Paterson 2005; Riaz *et al.* 2006; Rees, Selim & Ennis-King 2008; Slim & Ramakrishnan 2010; Kim & Choi 2012). (See also Elder 1968; Riaz *et al.* 2006; Pau *et al.* 2010; Elenius & Johannsen 2012; Slim *et al.* 2013.)

(c) Once convective fingers are macroscopic, they accelerate downwards with little lateral motion, stripping dense fluid from the interface and sharpening the concentration gradient at the upper boundary. This augments the dissolution flux, causing it to deviate from $\hat{t}^{-1/2}$ decay and grow to a local maximum, in a *flux-growth regime*. (See Elder 1968; Hassanzadeh *et al.* 2007; Rapaka *et al.* 2008; Pau *et al.* 2010; Kneafsey & Pruess 2011; Elenius & Johannsen 2012; Slim *et al.* 2013.)

(d) Once fingers are sufficiently long, they begin interacting with their neighbours in a *merging regime*. Pairs of fingers zip together from the root downwards and stunted fingers retreat. Several generations of such coarsening occur to form complex downwelling plumes. (See Riaz *et al.* 2006; Hassanzadeh *et al.* 2007; Pau *et al.* 2010; Backhaus *et al.* 2011; Slim *et al.* 2013.)

(e) As a result of this coarsening, the upper horizontal boundary layer between the remaining primary plumes becomes sufficiently thick to be unstable. New plumes form, only to be swept back into and be subsumed by the primary plumes. (See Riaz *et al.* 2006; Pau *et al.* 2010; Backhaus *et al.* 2011; Slim *et al.* 2013; Hewitt *et al.* 2013.) In the Hele-Shaw cell experimental study of Slim *et al.* (2013), this was hypothesized to be a separate *reinitiation regime*. During it, mergers had ceased.

(f) Finally plumes impact the lower boundary and the entire layer progressively saturates with dissolved solute in a $\mathscr{R}$-dependent *shut-down regime*. The horizontally averaged concentration field has a vertically well-mixed bulk with a gradually expanding upper horizontal boundary layer. Exploiting this structure, a box-model analysis based on a Howard-style (Howard 1964) phenomenology provides a good description of the flux. (See Hewitt *et al.* 2013; Slim *et al.* 2013.)

A number of key questions remain. First, there is limited data for the merging and reinitiation regimes, there are no clear transition times between them, and in the Hele-Shaw experiments the reinitiation regime was not observed as being clearly distinct from the shut-down regime. Secondly, the experiments may have suffered from finite-size effects, especially for the later, post-coarsening regimes. More intriguingly, for larger $\mathscr{R}$, a statistically constant flux regime has been identified in both experiments (Neufeld *et al.* 2010; Backhaus *et al.* 2011) and simulations (Pau *et al.* 2010; Lindeberg & Wessel-Berg 2011; Hidalgo *et al.* 2012). How does this regime fit into the above classification? Indeed, why does it exist (surprising given that the system is progressively saturating)? There is also disagreement over the value of the flux and whether it is layer-depth- (and thus $\mathscr{R}$-)dependent.

We use simulations to validate and expand on the regime picture portrayed above and extend it to significantly higher Rayleigh numbers. In particular, we eliminate the separate reinitiation regime postulated from the Hele-Shaw experiments: reinitiations begin once the gap between plumes has grown to sufficient size through mergers, a process that is markedly spatially heterogeneous. Once reinitiations occur everywhere, the flux becomes constant and we find it more appropriate to introduce a constant-flux regime after the merging regime. We observe a $\mathscr{R}$-independent flux (in contradiction to Neufeld *et al.* 2010; Backhaus *et al.* 2011), whose value is in excellent agreement with the value obtained numerically by Pau *et al.* (2010). The flux is maintained at this constant value after plumes hit the lower boundary and until information about the finite vertical extent of the layer reaches the upper boundary. The flow then transitions to a shut-down regime with similar properties to those described above. We present a first characterization of the constant-flux regime, and give a partial explanation for the behaviour. We also present new and more accurate details of all the regimes, and show that there are clear, quantitative delineations between them. Furthermore, we disentangle perturbation- and $\mathscr{R}$-dependent effects by presenting simulations for increasing $\mathscr{R}$ with identical noisy initial conditions and thus showing $\mathscr{R}$-independence until the plumes hit the lower boundary and perturbation-independence after the merging regime.

Our most significant practical result is a system of upscaled equations and boundary conditions governing the evolution in the constant-flux and shut-down regimes. These link the horizontally averaged concentration, vertical advective flux and plume widths. The equations are incomplete, missing an evolution equation for the plume widths that describes the complex merging process. However, making certain empirical assumptions, we find reasonably good quantitative agreement with simulated behaviour for both solutal and thermal convection.

For the partially permeable upper boundary, significantly less is known. Because fluid is exchanged with the overlying layer, there is an additional source of dense fluid and convective modes are less restricted. Thus onset of instability occurs substantially sooner (Slim & Ramakrishnan 2010), although the first mode that can become unstable spans the layer thickness and is unlikely to be excited with appreciable amplitude. In the extremal case of an infinitely permeable overlying layer, simulations at $\mathscr{R} = 2000$ show the flux to increase approximately fourfold over the impermeable case (Elenius, Nordbotten & Kalisch 2012). We extend our regime decomposition to the partially permeable case for select relative permeabilities in the overlying layer. Intriguingly, we find that the boundary-layer structure changes markedly from the impermeable case, but significant features of the bulk flow such as the plume widths and flux in the shut-down regime remain almost identical.

The paper is organized as follows. In § 2, we describe the governing equations, scalings and relevant global measures and discuss the initial noisy perturbation. In § 3, we consider the impermeable upper boundary scenario, describing relevant dynamical details and global measures of the flow in each regime. We also summarize transitions between the regimes and when the Rayleigh number matters. In § 4, we derive the upscaled equations and apply them to the constant-flux and shut-down regimes. In appendix D, we apply them to the companion thermal problem. In § 5, we show how the flow is modified with a partially permeable upper boundary and describe insights that can be gained for the impermeable scenario. We summarize the principal new results in § 6 and comment on their inclusion in geological CO_2-storage simulators.

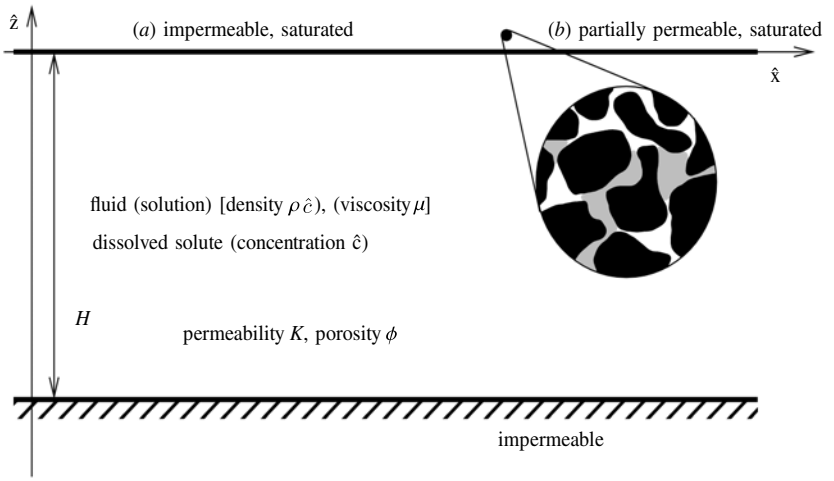

FIGURE 1. Configuration after solute is instantaneously introduced into the pore space above $\hat{z} = 0$. The boundary between the convecting layer $\hat{z} < 0$ and the separate-phase-solute bearing overlying layer $\hat{z} > 0$ is either (*a*) impermeable or (*b*) partially permeable to fluid flow. In the latter case, the inset sketches a possible pore-level configuration: black regions represent solid grains; grey regions represent separate-phase solute; and white regions represent solute-saturated fluid.

2. Formulation

Here we briefly describe the governing equations, scalings and important global measures. The impermeable upper boundary system is identical to that of previous studies; further details and justifications of assumptions for application to CO_2 storage are given by, for example, Ennis-King & Paterson (2005) and Slim & Ramakrishnan (2010). The permeable upper boundary scenario was previously formulated by Slim & Ramakrishnan (2010).

Consider a horizontal, two-dimensional, ideal porous layer of permeability K, porosity ϕ and thickness H as shown in figure 1. It is underlain by an impermeable lower layer. It is overlain by a solute-bearing upper layer in which the solute is instantaneously placed at time $\hat{t} = 0$ and which may be impermeable or partially permeable to fluid flow. We study the convective dissolution process in isolation, thus we assume there are no changes in the system's geometry, temperature or pressure. The layer is described by Cartesian coordinates $(\hat{x}, \hat{z})$, with $\hat{x}$ directed horizontally, $\hat{z}$ directed vertically upwards and $\hat{z} = 0$ coinciding with the boundary between the solute-bearing and convecting layers.

We assume inertialess, Boussinesq, incompressible Darcy flow through the medium

$$\hat{u} = -\frac{K}{\mu}\left(\hat{\nabla}\hat{p} + \rho(\hat{c})ge_z\right), \quad \hat{\nabla}\cdot\hat{u} = 0 \quad \text{in } -H < \hat{z} < 0, \tag{2.1}$$

where $\hat{u} = (\hat{u}, \hat{w})$ is the Darcy velocity, $\hat{p}$ pressure, g gravity and μ fluid viscosity. The density ρ is the only solute-dependent property. It depends linearly on the concentration $\hat{c}$ above the initial average

$$\rho = \rho_0 + \Delta\rho\frac{\hat{c}}{c_{sat}}, \tag{2.2}$$

where c_{sat} is the excess concentration at saturation, ρ_0 is the initial average density and $\Delta\rho$ is the maximum excess density.

Solute is redistributed by advection and diffusion

$$\phi\frac{\partial\hat{c}}{\partial\hat{t}}+\hat{u}\cdot\hat{\boldsymbol{\nabla}}\hat{c}=\phi D\hat{\nabla}^2\hat{c}\quad\text{in }-H<\hat{z}<0, \tag{2.3}$$

where D is the effective diffusivity.

The lower boundary is impenetrable to fluid and solute

$$\hat{w}=0,\quad \frac{\partial\hat{c}}{\partial\hat{z}}=0\quad\text{on }\hat{z}=-H. \tag{2.4}$$

The upper boundary is saturated

$$\hat{c}=c_{sat}\quad\text{on }\hat{z}=0 \tag{2.5}$$

and either impermeable or partially permeable to fluid flow. In the former case, we have

$$\hat{w}=0\quad\text{on }\hat{z}=0. \tag{2.6}$$

In the latter case, the overlying layer is taken to be infinitely thick and to have relative permeability $\mathscr{K}\geqslant 0$. We assume that fluid in the overlying layer is instantaneously saturated $\hat{c}=c_{sat}$, thus the equations governing flow are

$$\hat{u}=-\frac{\mathscr{K}K}{\mu}\left(\hat{\boldsymbol{\nabla}}\hat{p}+(\rho_0+\Delta\rho)ge_z\right),\quad \hat{\boldsymbol{\nabla}}\cdot\hat{u}=0\quad\text{in }\hat{z}>0, \tag{2.7}$$

with interfacial conditions

$$[\hat{w}]=0,\quad [\hat{p}]=0\quad\text{on }\hat{z}=0, \tag{2.8}$$

where $[\cdot]$ indicates a jump in the bracketed quantity.

We take the system to be periodic in $\hat{x}$ with period $\hat{W}$.

2.1. *Scalings*

A natural velocity scale for the flow is the speed with which a fully saturated fluid parcel falls, $\mathscr{U}=K\Delta\rho g/\mu$. Natural length scales are the length over which advection and diffusion balance $\mathscr{L}=\phi D/\mathscr{U}$ and the layer thickness H. We choose to rescale by $\mathscr{L}$, because then the role of $\mathscr{R}$ becomes clear. We set

$$\hat{u}=\mathscr{U}u,\quad \hat{p}+\rho_0 g\hat{z}=\frac{\mu\mathscr{U}\mathscr{L}}{K}p,\quad \hat{c}=c_{sat}c,\quad \hat{x}=\mathscr{L}x\quad\text{and}\quad \hat{t}=\frac{\phi\mathscr{L}}{\mathscr{U}}t \tag{2.9}$$

to generate the parameter-free governing equations

$$u=-\boldsymbol{\nabla}p-ce_z,\quad \nabla\cdot u=0\quad\text{and}\quad \frac{\partial c}{\partial t}+u\cdot\boldsymbol{\nabla}c=\nabla^2c. \tag{2.10}$$

Lower boundary conditions are

$$w=0,\quad \frac{\partial c}{\partial z}=0\quad\text{on }z=-\mathscr{R}. \tag{2.11}$$

Thus, the Rayleigh number

$$\mathscr{R}=\frac{HKg\Delta\rho}{\mu\phi D} \tag{2.12}$$

only appears as the location of the lower boundary and is interpreted as the dimensionless layer thickness. The impermeable upper boundary conditions are

$$w = 0, \quad c = 1 \quad \text{on } z = 0. \tag{2.13}$$

In the permeable upper boundary scenario, the rescaled equations in the overlying layer become

$$u = -\mathscr{K}\left(\nabla p + e_z\right), \quad \nabla \cdot u = 0, \tag{2.14}$$

with interfacial conditions

$$[w] = 0, \quad [p] = 0, \quad c = 1 \quad \text{on } z = 0. \tag{2.15}$$

We impose periodic boundary conditions on $x = 0$ and $x = \hat{W}/\mathscr{L} = W$.

We solve this system numerically using a spectral method for the impermeable case and a compact finite-difference method for the permeable one as described in appendix A. We set the domain width $W = 10^5$ independent of Rayleigh number. This gives an aspect ratio of two at the highest $\mathscr{R}$ considered.

2.2. *Initial condition*

We initiate instability by adding noise to the diffusive concentration field

$$c_{diff} = 1 + \operatorname{erf}(z/2\sqrt{t}) \quad \text{for } z < 0, \tag{2.16}$$

at time $t = 1$. To identify precisely when $\mathscr{R}$ effects influence the solution, we must be able to distinguish them from perturbation effects. Thus, we create a random-but-reproducible initial condition across different $\mathscr{R}$ as follows. We initialize the perturbation on a coarse mesh ($\Delta x = 20$, $\Delta z = 10$) from a uniform distribution $(-1, 1)$ with a repeatable seed. We then modulate the thus-generated field by $\epsilon\sqrt{0.002}z \exp(0.5 - 0.001z^2)$ to localize the perturbation to the interface, where the prescribed value ϵ is the largest possible amplitude and we arbitrarily choose a localization parameter 0.001. Finally, we use cubic splines to interpolate the field onto the computational, physical collocation mesh. Note that, although generally we may expect the perturbation to be restricted to the upper regions, we do not expect it to be constrained to the diffusive boundary layer, which is arbitrarily thin for $t \to 0$.

2.3. *Global measures*

A number of global measures are useful for quantifying the flow. The most important is the dissolution flux, the rate at which solute dissolves from the upper boundary at $z = 0$. Dimensionally, it is given by

$$\hat{F}(\hat{t}) = \frac{\phi D}{\hat{W}} \int_0^{\hat{W}} \left.\frac{\partial \hat{c}}{\partial \hat{z}}\right|_{\hat{z}=0} \mathrm{d}\hat{x}. \tag{2.17}$$

Setting $\hat{F} = \mathscr{U} c_{sat} F$, this rescales to

$$F(t) = \frac{1}{W} \int_0^{W} \left.\frac{\partial c}{\partial z}\right|_{z=0} \mathrm{d}x. \tag{2.18}$$

Note that a constant value of F thus implies a dimensional flux that is independent of the diffusivity.

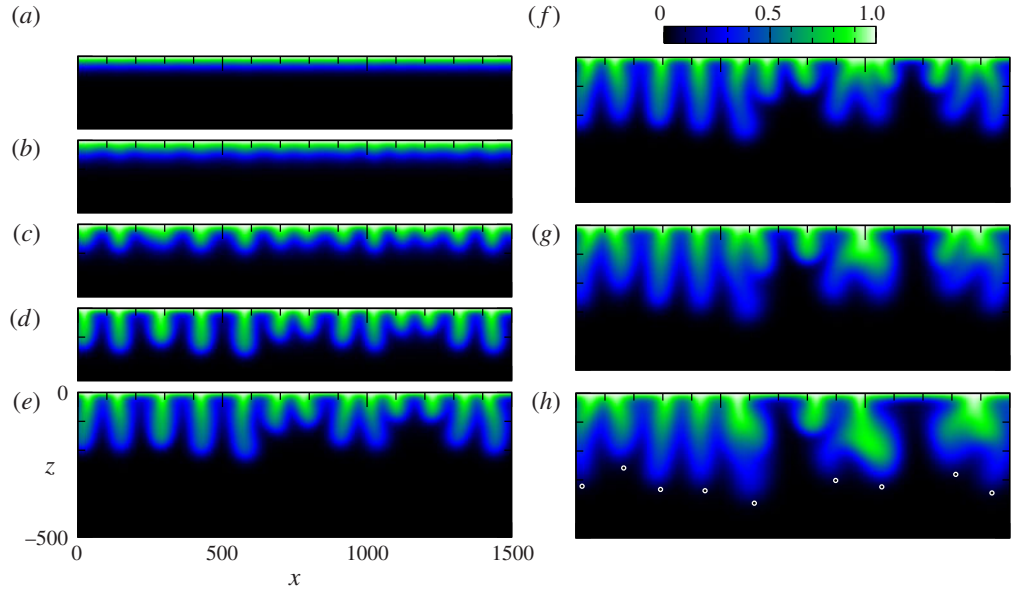

FIGURE 2. (Colour online) Simulated concentration profiles at early times for Rayleigh numbers $\mathscr{R} \gtrsim 500$ and initial perturbation amplitude $\epsilon = 0.01$ (specifically $\mathscr{R} = 5 \times 10^4$, with the same initial condition as later figures): (*a*) $t = 500$ (lg); (*b*) $t = 1000$ (lg); (*c*) $t = 1500$ (fg); (*d*) $t = 2000$ (fg); (*e*) $t = 2500$ (m); (*f*) $t = 3000$ (m); (*g*) $t = 3500$ (m); (*h*) $t = 4000$ (m). The dots in (*h*) show the location of fingertips. Note that the scale is the same in all plots and that only a small portion of the domain is shown (the bottom of the layer is far below and does not yet influence dynamics).

At early times, it is useful to consider the amplitude of the perturbation away from pure diffusion. We measure this using the mean square deviation

$$A(t) = \frac{1}{W} \int_{-\mathscr{R}}^{0} \int_{0}^{W} (c - c_{diff})^2 \, \mathrm{d}x \, \mathrm{d}z. \tag{2.19}$$

The full diffusive solution is given by, for example, Ennis-King & Paterson (2005). The error function profile (2.16) is an excellent approximation for c_{diff} provided $t \lesssim \mathscr{R}^2/36$.

We also report fingertip and plumetip locations and define these as minima of the $c = 0.05$ contour (examples are shown in figures 2*h* and 3*d*).

Horizontally averaged quantities are useful for characterizing the later regimes. These are defined by

$$\langle a \rangle (z, t) = \frac{1}{W} \int_{0}^{W} a(x, z, t) \, \mathrm{d}x \tag{2.20}$$

for some variable a. We particularly focus on $\langle c \rangle$, the horizontally averaged concentration, and $\langle c'^2 \rangle$, the mean square of the fluctuations $c' = c - \langle c \rangle$. The latter can be thought of as the 'strength' of plumes.

A final useful measure is the average width of fingers and plumes $\omega = \pi/k$, where we define

$$k = \sqrt{\langle (\partial c'/\partial x)^2 \rangle / \langle c'^2 \rangle}, \tag{2.21}$$

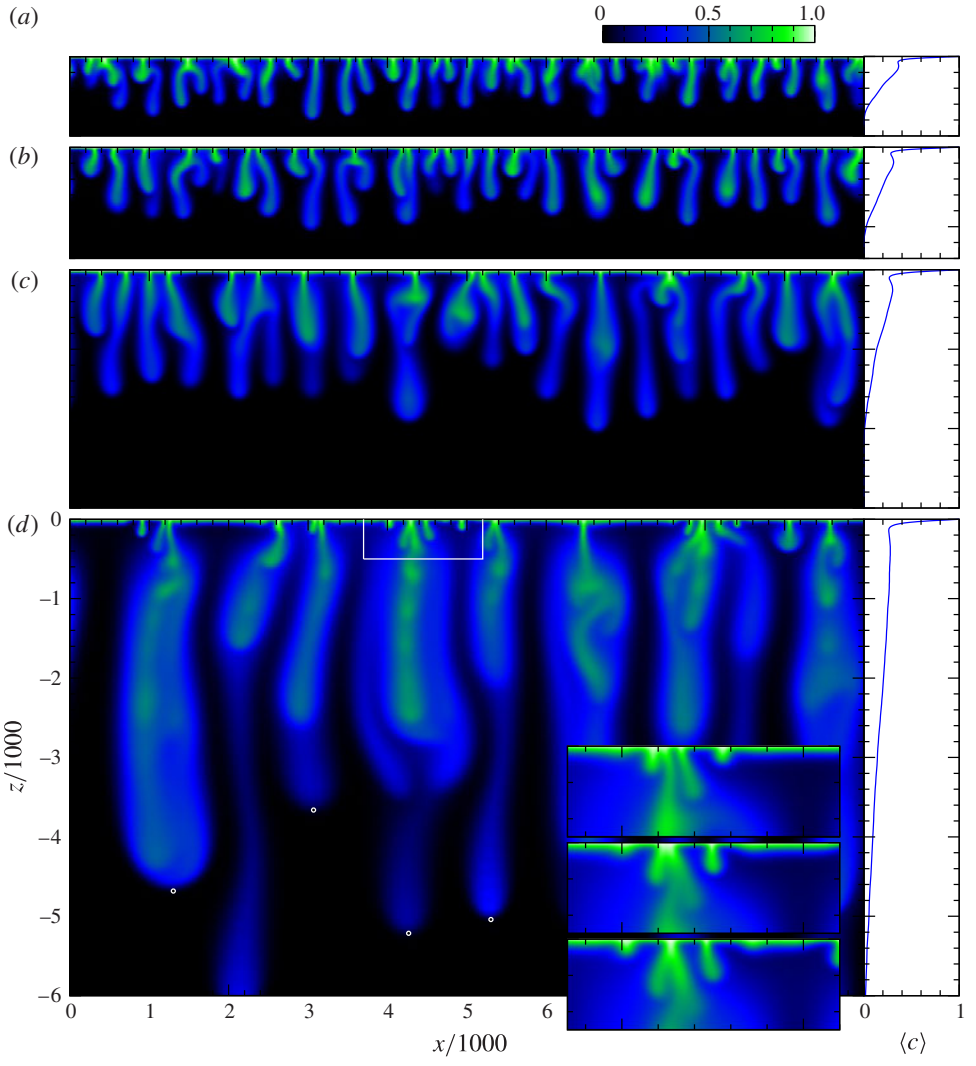

FIGURE 3. (Colour online) Simulated concentration profiles at intermediate times for $\mathscr{R} = 5 \times 10^4$ and $\epsilon = 0.01$: (*a*) $t = 6500$ (m); (*b*) $t = 8500$ (m); (*c*) $t = 14\,500$ (m); (*d*) $t = 50\,500$ (cf). Panels on the right give the horizontally averaged concentration profile. In (*d*), the insets show a close-up of reinitiations at times $t = 44\,500$, $46\,500$ and $48\,500$ (top to bottom) in the boxed region. In (*d*), the dots show the location of fingertips. Note that the spatial scale is the same in all plots and that only a portion of the domain is shown (the bottom boundary is at $z/1000 = -50$).

essentially the root mean square of the wavenumbers in a Fourier decomposition. (See also appendix B.)

3. The impermeable upper boundary

We begin with the more commonly studied scenario of a flow-impermeable upper boundary. Snapshots for an exemplar simulation with $\mathscr{R} = 5 \times 10^4$ are shown

in figures 2–4 and in supplementary movies available online at http://dx.doi.org/10.1017/jfm.2013.673. Figure 2 shows concentration profiles at early times for a small region near the upper boundary. Figure 3 shows profiles at intermediate times for a broader region. Figure 4 shows profiles at later times for the full domain. These illustrate the regime progression described in the introduction: initially there is the diffusive regime (similar to figure 2*a*). In the linear-growth regime (labelled 'lg'), faint perturbations appear on the diffusive boundary layer beneath $z = 0$ (figure 2*a,b*). During the flux-growth regime (labelled 'fg'), macroscopic fingers are apparent that propagate primarily vertically (figure 2*c,d*). In the merging regime (labelled 'm'), fingers begin lateral migration and merge to form complex downwelling plumes (figures 2*e–h* and 3*a–c*). In the constant-flux regime (labelled 'cf'), small protoplumes are reinitiated on the diffusive boundary layer below $z = 0$ and are swept into primary plumes (figure 3*d* and insets). The primary plumes propagate downwards, impact the lower boundary and spread laterally as gravity currents (figure 4*a*). These progressively thicken. Once the information about the finite extent of the layer reaches the top, the entire layer progressively saturates in the shut-down regime (labelled 'sd' and represented by figure 4*b*).

In the following subsections, we give further physical descriptions and interpretation of the different regimes, together with quantitative details. One of our aims is to show that a clear quantitative delineation exists between most of the regimes. To show this distinctly, we plot some of the global measures described in § 2.3 concurrently in figures 5 and 6 for early and late times, respectively.

3.1. *The diffusive regime (d)*

Initially, the flow appears purely diffusive. Although denser fluid is progressively building up over lighter by diffusion of solute across the upper boundary, not enough has accumulated to overcome the smoothing effect of diffusion within the layer and sustain a growing convection cell. Perturbations away from the pure one-dimensional diffusion profile decay. This is quantified by the amplitude of the perturbations $A(t)$ decaying (figure 5*a*). The flux decays diffusively (figure 5*b*) as

$$F(t) = 1/\sqrt{\pi t}. \tag{3.1}$$

3.2. *The linear-growth regime (lg)*

The second regime is linear growth. Eventually, enough dense material accumulates beneath $z = 0$ for convection to commence. Faint perturbations become apparent on the diffusive boundary layer (figure 2*a,b*).

We define the linear-onset time as the time when the perturbation amplitude $A(t)$ first starts to grow, $t = 116$ for the exemplar simulation (figure 5*a*). This appears rather late compared with the earliest unstable mode prediction. However, it is a global measure of onset and growth of select modes can be masked by decay of many. Figure 7 shows onset time decomposed by wavenumber. Short waves are suppressed by lateral diffusion, while long waves require more dense fluid to grow than has accumulated: intermediate wavelengths between 80 and 140 are the first to become unstable, and do so at $t \approx 55$. This is in reasonable agreement with earliest unstable mode theory ($t = 47.9$; Slim & Ramakrishnan 2010). After onset, the same intermediate wavelengths remain dominant and amplify quasi-exponentially as

$$A(t) \propto \epsilon^2 \exp(\sigma t), \tag{3.2}$$

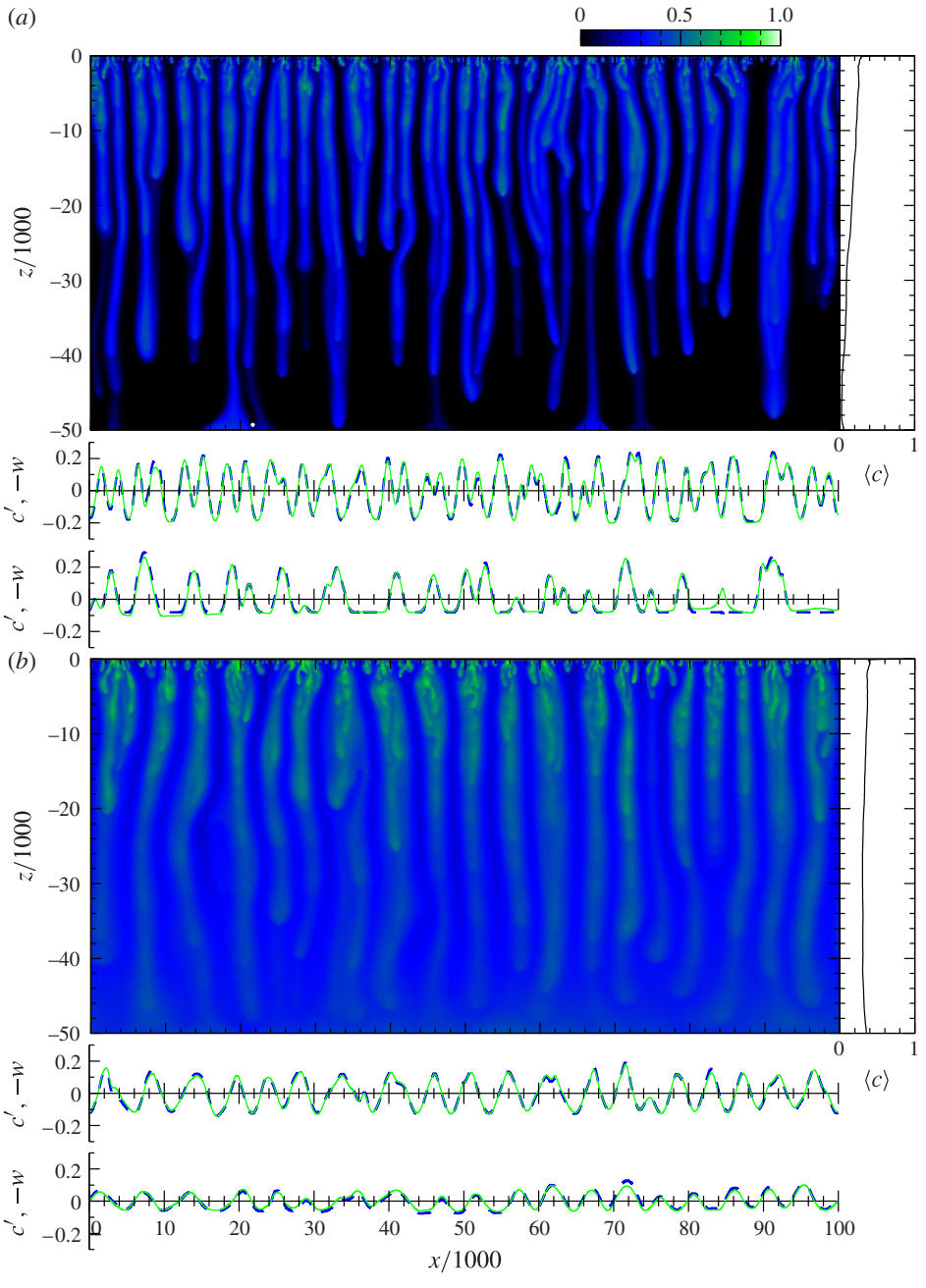

FIGURE 4. (Colour online) Simulated concentration profiles at late times for $\mathscr{R} = 5 \times 10^4$: (*a*) $t = 8\mathscr{R} = 4 \times 10^5$ (cf); (*b*) $t = 20\mathscr{R} = 10^6$ (sd). Beneath each snapshot, the concentration fluctuation profile (bold, dashed dark/blue curves) and vertical velocity profile (solid pale/green curves) are shown on slices at $z = -15\,000$ and $z = -35\,000$. Figures on the right give the horizontally averaged concentration profile. Note that the spatial scale is the same in all plots. The full domain is shown. In (*a*) the solid white disc near the lower boundary is the bottom of a shrinking pool of $c < 0.05$ fluid (see figure 6*b*).

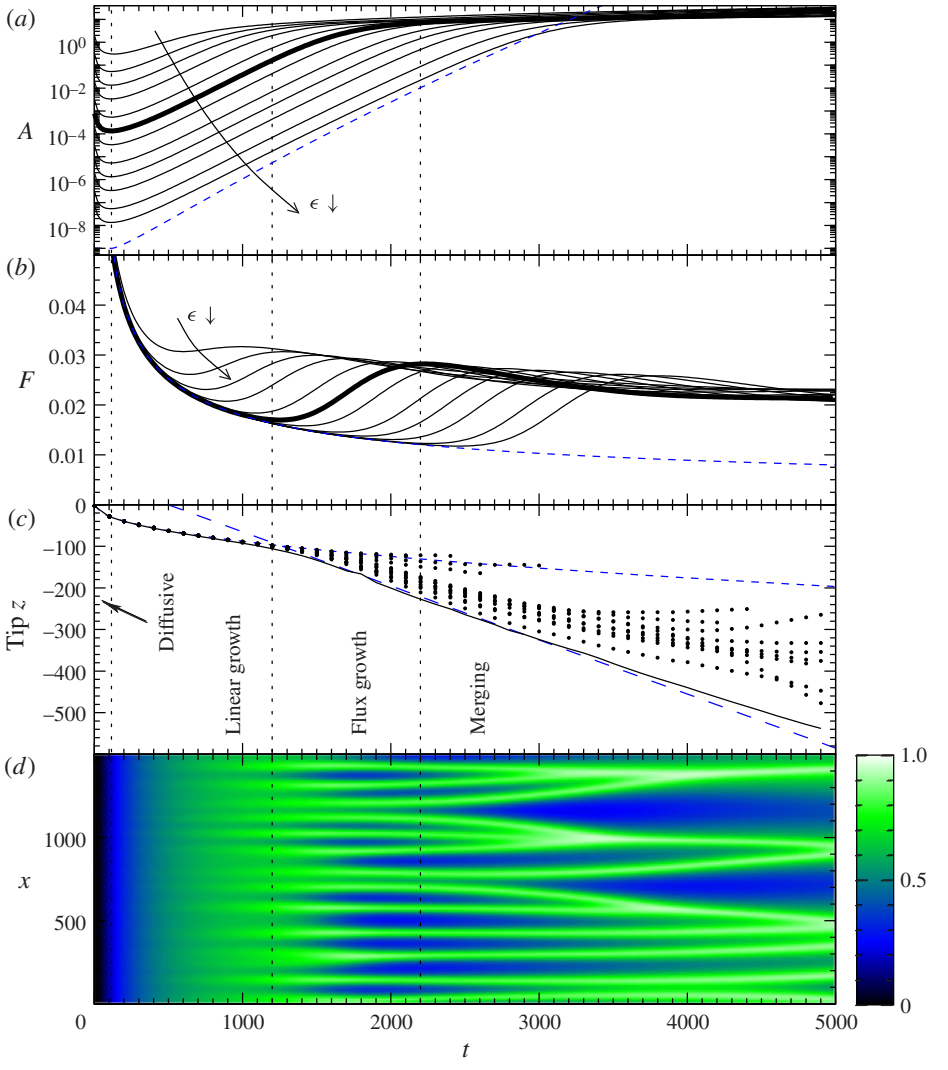

FIGURE 5. (Colour online) Global measures at early times. (*a*) Amplitude as defined by (2.19). The curve for initial amplitude $\epsilon = 0.01$ is bold and various additional initial amplitudes from $\epsilon = 0.0001$ to 0.2 are also plotted. The dashed curve is the theoretical prediction for the maximum possible amplification of infinitesimal disturbances across all wavenumbers, following the approach of Rapaka *et al.* (2008). An initial amplitude of 10^{-9} is plotted. (*b*) Dissolution flux of solute into solution, with the curve for $\epsilon = 0.01$ in bold and the same selection of additional initial amplitudes. The dashed curve is the purely diffusive behaviour given by (3.1). (*c*) Fingertip locations for $\epsilon = 0.01$ defined as minima of the $c = 0.05$ contour for the tips shown in figure 2 (points) together with the maximum extent of all fingertips (solid curve). The short-dashed curve is the location of the $c = 0.05$ contour for pure diffusion given by $z(c = 0.05) = -2.78\sqrt{t}$ and the long-dashed line is $-0.13(t - 500)$. (*d*) Concentration profile on $z = -20$ for $\epsilon = 0.01$ to illustrate root movement. Darker/bluer regions correspond to low concentrations and paler/greener to high concentrations.

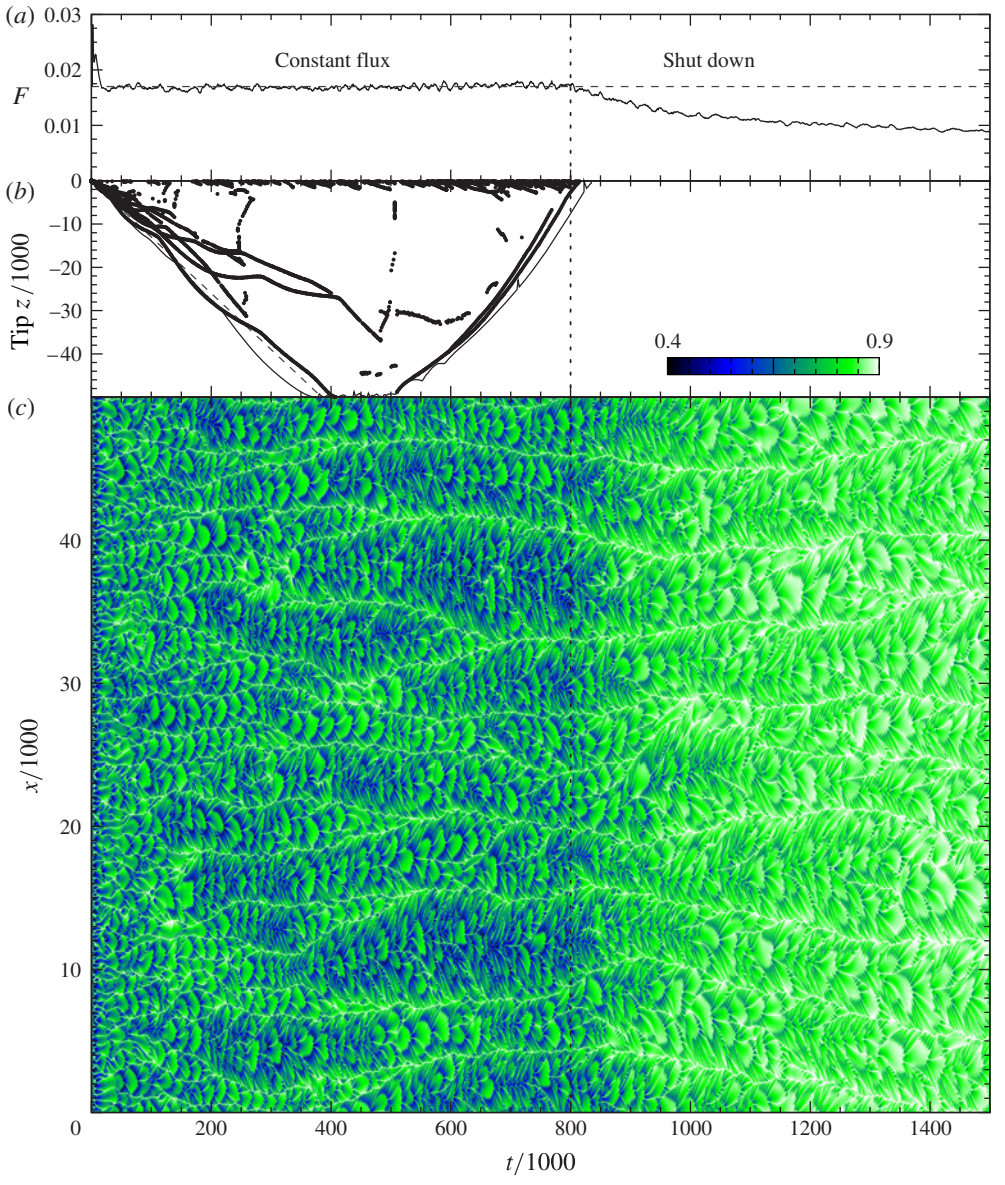

FIGURE 6. (Colour online) Intermediate and long time global measures for $\mathscr{R} = 5 \times 10^4$ and initial amplitude $\epsilon = 0.01$: (*a*) dissolution flux of solute into solution; (*b*) a selection of tip locations; and (*c*) the concentration profile on $z = -20$ to illustrate root motion and merging. In (*a*), the dashed line is the value $F = 0.017$ from (3.3). In (*b*), the dashed line is $z = -w_0 t$ as implied by the self-similar wedge approximation (3.4). The upwardly propagating 'plumetips' are the bottoms of shrinking pools of $c < 0.05$ fluid; an example is shown by a disc in figure 4(*a*). The solid curve is the envelope over all plumes. In (*c*), darker/bluer regions correspond to anomalously low concentrations and paler/greener to anomalously high concentrations.

with $\sigma \approx 0.007$. This growth rate is in reasonable agreement with maximum amplification theory (Rapaka *et al.* 2008), as shown in figure 5(*a*).

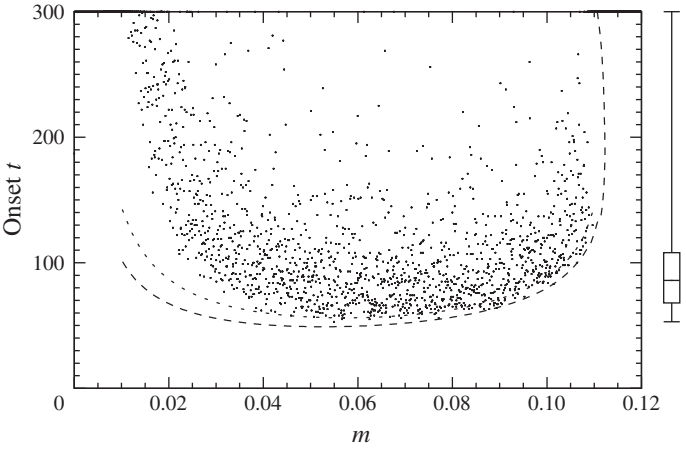

FIGURE 7. Onset time for amplitude growth decomposed by Fourier wavenumber m for $\mathscr{R} = 1000$ and initial amplitude $\epsilon = 0.01$ (although the plot is indistinguishable for $\epsilon \lesssim 0.1$). The dotted curve is the quasi-steady state approximation and the dashed curve is the lower bound prediction (Slim & Ramakrishnan 2010). The box-and-whisker plot on the right gives the range of onset times, the quartiles and the median for intermediate wavenumbers $k \in (0.05, 0.07)$.

The details of this regime are sensitive to the structure of the initial perturbation (although independent of the amplitude, provided $\epsilon \lesssim 0.1$). Contributions of wavelengths around 80 to 140 are key: if they are negligible then onset is delayed and the emerging fingers are coarser grained. Elenius & Johannsen (2012) give an extensive discussion of sensitivity to initial conditions.

Until the end of this regime, convective fingers are almost imperceptible and mass transport is dominated by diffusion, with the flux still well-approximated by (3.1) (figure 5*b*).

3.3. *The flux-growth regime (fg)*

The third regime is flux growth. Fingers are now apparent and begin to influence mass transport: they efficiently strip dense material from the interface that accumulated diffusively during linear growth. This sharpens the diffusive boundary layer beneath $z = 0$ (see figure 2*b–d*) and thus increases the dissolution flux.

Flux growth is arguably the most practical measure of convective onset and is equivalent to the Schmidt–Milverton principal for thermal convection (Chandrasekhar 1961). For the exemplar simulation, it occurs at $t = 1200$ (figure 5*b*). The flux then increases until $t = 2200$. Both the minimum and maximum flux and times at which they are achieved depend sensitively on the initial perturbation amplitude (see figure 5(*b*) and Elenius & Johannsen 2012). They also depend on the perturbation structure. For example, shorter wavelength perturbations begin growing sooner. Therefore, such perturbations have less excess material and generate less intense convection. As a result, they do not over-thin the boundary layer significantly and a smaller flux maximum is achieved.

Throughout, fingers strengthen and elongate. At the beginning of the regime, vertical segregation of the fingertips begins (figure 5*c*), with the pioneers accelerating and achieving a speed of approximately 0.1 as mass transport becomes dominated by advection. A key characteristic is that fingers have limited lateral motion, as indicated by the essentially immobile roots (figure 5*d*).

3.4. *The merging regime (m)*

The fourth regime is merging. Individual fingers generate a global velocity field and thus influence one another's motion. Coinciding with the time of maximum flux, this becomes a significant effect and fingers begin to interact. Where a finger lags behind, it can be forced to retreat by the upward return flow generated by its faster neighbours. Where fingers are comparable in length, pairs that are slightly closer together than their outer neighbours get pushed closer by the upwelling flow exterior to both impinging on the upper boundary and spreading laterally. The two fingers migrate towards one another and ultimately zip together. This is seen in the concentration snapshots in figure 2(*e–h*) and the evolution of finger roots shown in figure 5(*d*). The zipping occurs from the root downwards. Once the fingers partially zip together, one effectively channels all the flow and solute while the other diffusively withers. Multiple generations of this coarsening process occur, although becoming rarer as the finger spacing increases and roots must traverse a greater distance before colliding and combining. Progressively the flow transitions to a system of downwelling dense plumes interwoven with broader regions of upwelling fresh fluid (figure 3*a–c*).

As the plume spacing increases, the diffusive boundary layer below $z = 0$ thickens slightly. This results in a decreased concentration gradient in the boundary layer and thus progressively reduces the dissolution flux.

This regime can be thought of as a reorganizational one. It marks the end of the strongly initial-condition-dependent phase and commencement of an effectively universal one in which variations due to any differences in the initial conditions are less than chaotic fluctuations: the empirical fits that we present for subsequent regimes were identical across multiple realizations.

3.5. *The constant-flux regime (cf)*

The fifth regime is constant flux. Once the plumes are sufficiently widely spaced through mergers, the diffusive boundary layer below $z = 0$ between them becomes sufficiently thick to be unstable. A new regime begins whose prominent feature is reinitiation of small 'protoplumes' on this boundary layer (using the nomenclature of Hewitt *et al.* 2012, 2013). These are rapidly swept into and merge with the existing primary plumes by the upwelling flow between them (insets to figure 3(*d*); see also Hewitt *et al.* 2012). Reinitiations are generated in pulses, with the first protoplume forming close to a primary plume and subsequent protoplumes generated outside their predecessors (figure 6*c*). This continues until a protoplume is generated almost at the stagnation point of the upflow between two bounding primary plumes. This protoplume persists for longer. It is usually swept into an existing primary plume eventually, resetting the cascade. Very rarely it survives to form a new primary plume.

These protoplume pulses can be interpreted as the diffusive boundary layer below $z = 0$ becoming marginally stable (Howard 1964; Doering & Constantin 1998): if the boundary layer is too thin, then it thickens by diffusion, while if it is too thick, a protoplume pulse strips the excess dense material. Note that the timing for reaching this state is spatially heterogeneous and thus the transition time between the merging and constant-flux regimes is murky. For the exemplar simulation it occurs between 16 000 and 40 000.

Mergers between primary plumes continue in this regime. However, they become increasingly rare. A new mechanism for mergers, and increasingly the dominant one, is slip-streaming: lagging plumes are drawn into their further-advanced neighbours. This cuts off the supply of upwelling fresh fluid between them and they progressively zip together from the tip upwards.

A key observation about the primary plumes is that they are long and thin. Structurally they appear complex: episodic mergers of protoplumes into them generate negatively buoyant blobs that descend and diffuse on a background downwelling. In addition, during mergers of primary plumes, there can be multiple maxima on horizontal slices within a given plume. In the upper portions of the domain, plumes exist everywhere with regions of upwelling fresher fluid having a width comparable to the plumes (figure 4*a*). In the lower portions of the affected domain, the fluid is mostly fresh, with a few isolated pioneer plumes. These decelerate in time, eventually nearly stagnating or even retreating before an injection of dense fluid from a trailing plume merging into it causes it to advance again (this process results in the 'bouncing' of plume tips in figure 6*b*). After these pioneer plumes impact the bottom boundary, they spread locally as dense gravity currents (figure 4*a*). These progressively pervade the entire layer in a manner similar to a filling-box mechanism (Turner 1973) (illustrated, for example, by the shrinking pools of $c < 0.05$ fluid beneath the interface in figure 6*b*). Once the information about the finite thickness of the layer has reached the top boundary, the constant-flux regime ends and the flow transitions to a final, shut-down regime.

3.5.1. *The flux and other horizontally averaged quantities*

Turning to a more quantitative description of this regime, the key characteristic is that the flux is statistically constant throughout (figure 6*a*)

$$F = 0.017, \tag{3.3}$$

(an empirical fit). This value is in excellent agreement with that obtained in two-dimensional simulations by Pau *et al.* (2010). A constant flux is remarkable, given that the layer beneath is progressively saturating and suggests that the plumes adapt efficiently to remove and redistribute the incoming dense fluid. We provide a partial mathematical justification below.

Although the plumes appear dynamically complex, they have a surprisingly simple horizontally averaged behaviour. The 'bouncing' plumetips in the pioneer region propagate downwards at an approximately constant speed on average, $w_0 \approx 0.13$ (an empirical fit; see figure 6*b*). Above them, the horizontally averaged concentration profile stretches almost as the self-similar wedge

$$\langle c \rangle = c_0[1 + z/(w_0 t)] \quad \text{for } -w_0 < z/t < 0, \tag{3.4}$$

where $c_0 \approx 0.27$ (an empirical fit; see figure 8*a*). Note that there is a slight break-in-slope at $z/t \approx -0.08$ corresponding to the top of the pioneer plume region.

The average plume width increases proportionally to $\sqrt{t}$. The prefactor has vertical structure in z/t: because merging occurs at plume tips, it decreases from approximately π for the pioneers in $z/t \lesssim -0.08$ to $\pi/\sqrt{2}$ at the roots (figure 8*c*).

After impact, the filling-box mechanism is manifested by an upwardly propagating wedge overriding the downwardly propagating wedge (3.4), leaving the latter unaffected (figure 8*a*). The plume width appears to continue to scale as $\sqrt{t}$ (figure 8*c*), although the post-impact subregime is too short to say so definitively. At $z = -\mathscr{R}$, the gravity currents nearly homogenize the fluid and the inferred 'plume widths' are nearly infinite (figure 8*c*).

Motivated by the simplicity of the horizontally averaged quantities and exploiting the slenderness of the plumes, we shall develop horizontally averaged equations governing the dynamics in § 4.

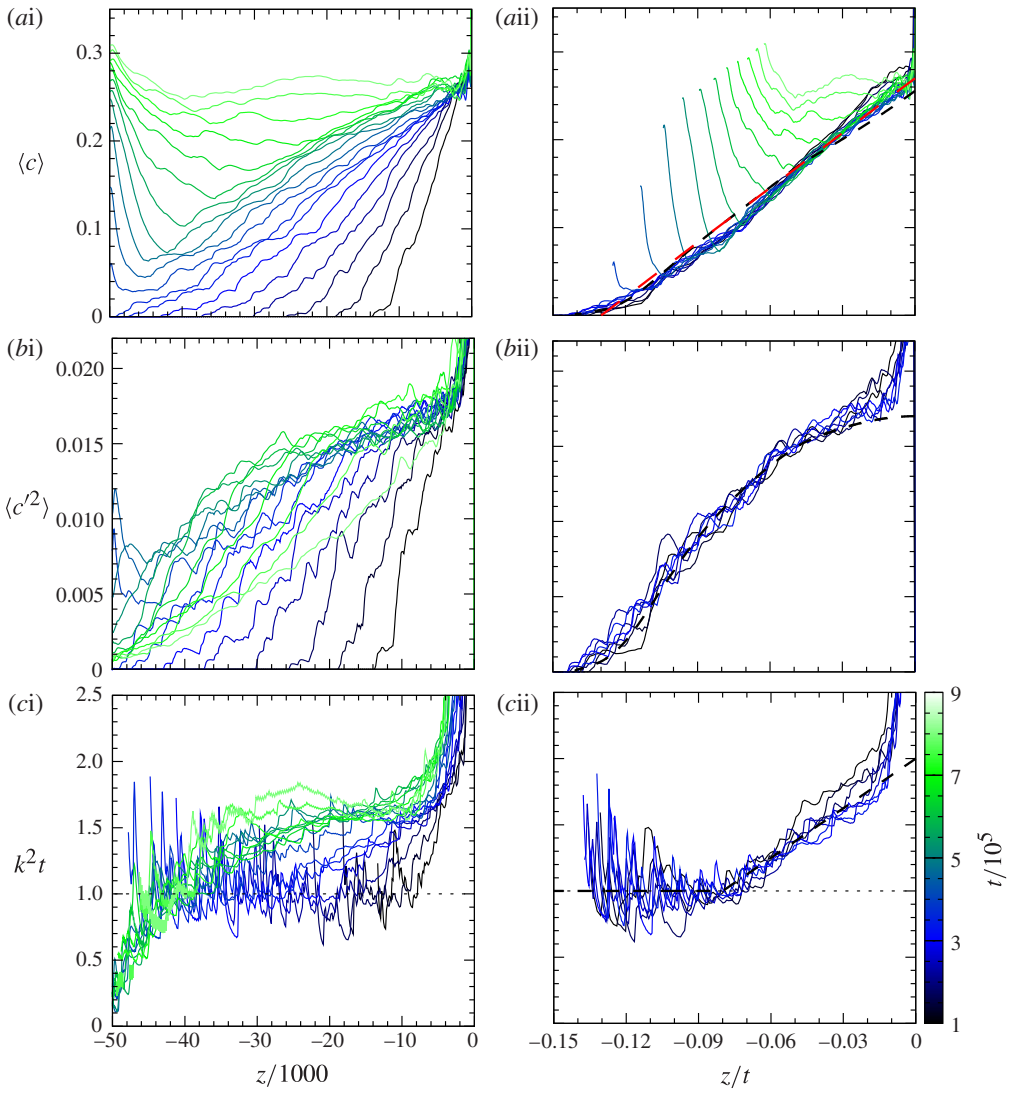

FIGURE 8. (Colour online) Solutions in the constant-flux regime for $\mathscr{R} = 5 \times 10^4$: horizontally averaged (*a*) concentration, (*b*) mean-square fluctuations and (*c*) wavenumber for times between $t = 10^5$ (darker/bluer curves) and 8×10^5 (paler/greener curves). Left figures (i) are versus the vertical coordinate z and right figures (ii) are versus the similarity variable z/t. The long-dashed (red online) line in (*a*ii) is the self-similar wedge approximation (3.4). The long-dashed bold black curves in (*a*ii) and (*b*ii) are the similarity solution of the upscaled equations of § 4, with the approximation used for k^2t shown in (*c*ii).

3.5.2. *Scalings revisited*

We can give some justification for a similarity solution for horizontally averaged quantities by considering the length scales relevant during plume evolution. In the present regime, the plumes are very long and so vertical diffusion becomes negligible. Therefore, the advection–diffusion length $\mathscr{L}$ used to rescale the governing equations in § 2.1 is no longer directly relevant. The layer thickness H is not yet relevant. Thus,

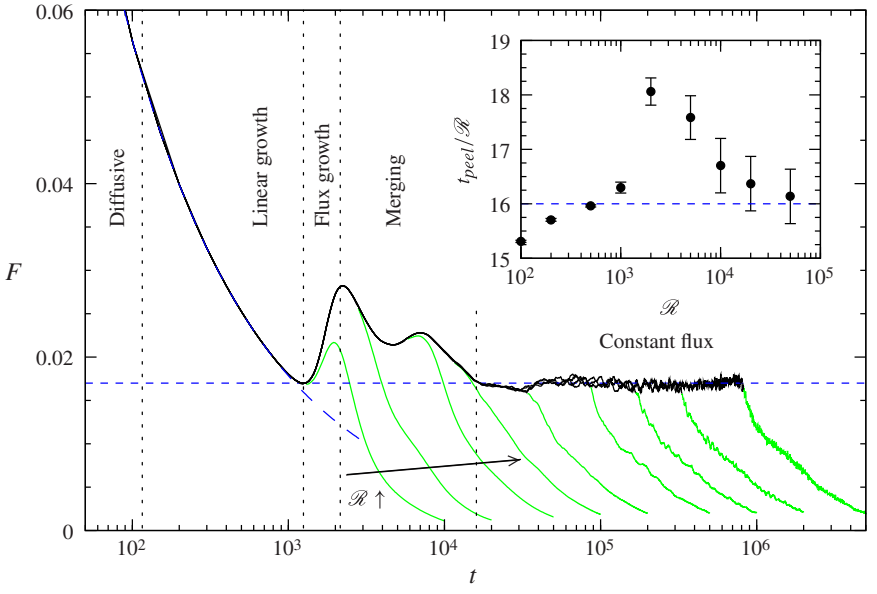

FIGURE 9. (Colour online) The dissolution flux versus time for Rayleigh numbers $\mathscr{R} = 100$, 200, 500, 1000, 2000, 5000, 10^4, 2×10^4 and 5×10^4. The first five dynamical regimes (diffusion through constant flux) are delineated. Transition to the shut-down regime for each $\mathscr{R}$ is indicated by the black curve becoming paler/greener. The long-dashed curve is the purely diffusive flux (3.1). The short-dashed line is the constant-flux regime value $F = 0.017$ from (3.3). The inset shows the time of peel-off t_{peel} to the shut-down regime as a function of $\mathscr{R}$ with the approximation $t_{peel} = 16\mathscr{R}$.

there is no apparent vertical length scale, and we may expect (Barenblatt 1996) a similarity solution in $\hat{z}/(\mathscr{U}\hat{t}) = z/t$. This argument is only valid if there is also no horizontal length scale. The horizontal wavenumber is set by a complex interplay between the induced horizontal velocity field and horizontal diffusion that controls merging and thus a length scale might be expected. Surprisingly, the observed scaling is the purely diffusive $(D\hat{t})^{1/2}$, implying there is no length scale and so a similarity solution is possible. How this scaling arises is unclear (see also Hewitt *et al.* 2012). Note that a similarity solution of this form implies a constant flux.

3.6. *When and how do H and $\mathscr{R}$ matter?*

Before plumes impact the base, the flow is parameter-independent: the only role of $\mathscr{R}$ is to determine how many of the $\mathscr{R}$-independent regimes described above are encountered. After impact, the top portion of the solution is still universal, until information about the bottom boundary has propagated to the top. This universality is perhaps most apparent in the flux (figure 9): for a repeatable noisy initial condition, the curves for different $\mathscr{R}$ all overlap until one by one they peel off and commence decay as the layer saturates and convection shuts down. (At longer times, the overlap is statistical rather than exact because tiny feedback from the large-scale flow results in chaotic variations.) Similarly, the evolution of the concentration profile on a slice just beneath the upper boundary (figure 10) is identical.

After plumes impact the bottom boundary, the layer thickness H becomes a relevant length scale. Similarly to the argument for the existence of a similarity solution above,

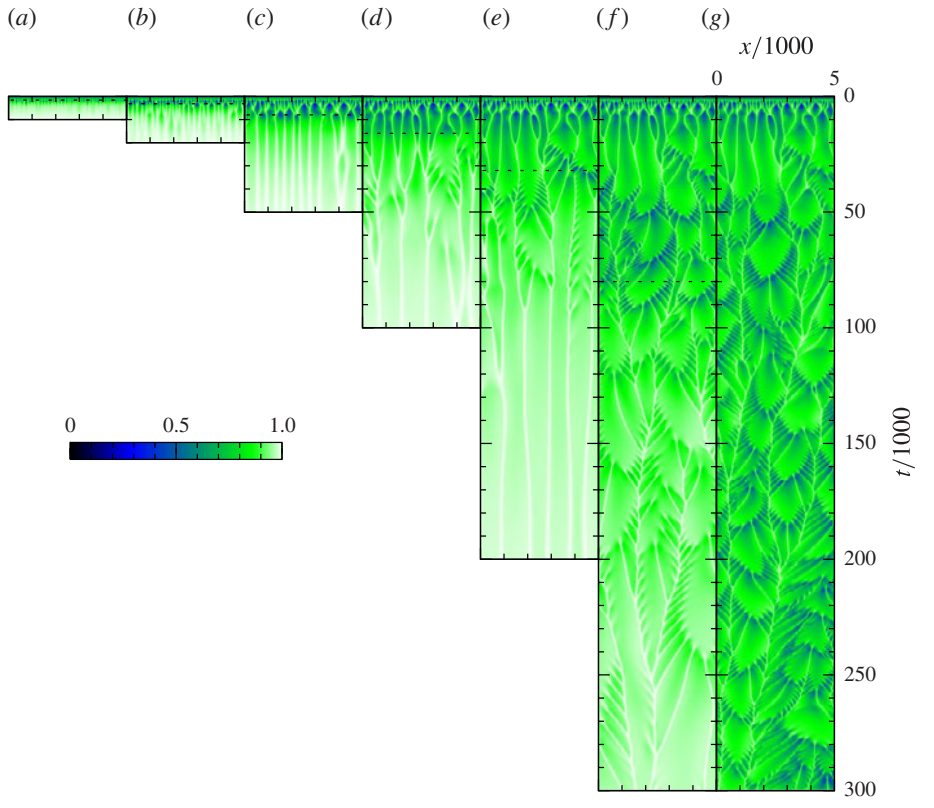

FIGURE 10. (Colour online) Evolution in time of the concentration profile on $z = -20$ for various Rayleigh numbers:(*a*) $\mathscr{R} = 100$; (*b*) $\mathscr{R} = 200$; (*c*) $\mathscr{R} = 500$; (*d*) $\mathscr{R} = 1000$; (*e*) $\mathscr{R} = 2000$; (*f*) $\mathscr{R} = 5000$; (*g*) $\mathscr{R} = 5 \times 10^4$. The dashed lines indicate the time of transition to the shut-down regime.

we might now expect results to be universal if the governing equations (2.1)–(2.6) are rescaled by H rather than $\mathscr{L}$. This is equivalent to considering independent variables $x/\mathscr{R}$, $z/\mathscr{R}$ and $t/\mathscr{R}$. This indeed yields universal results for the time that plumes impact the base, $t \approx 8\mathscr{R}$, and the end of the constant-flux regime, $t \approx 16\mathscr{R}$ (figure 9 inset). It also provides an excellent collapse for the flux in the shut-down regime (figure 11*d*) and a good collapse of the horizontally averaged concentration (not shown). However, for this argument to be entirely valid, no horizontal length scale should be apparent. Some of the implications of this assumption are found to be incorrect, for example the wavenumber in thermal convection should then scale as $\mathscr{R}^{-1/2}$, whereas the exponent is actually observed to be closer to $-3/5$ (Hewitt *et al.* 2012).

3.7. *The shut-down regime (sd)*

The dynamical nature of the sixth and final, shut-down regime remains that of the regime before transition (illustrated in the root behaviour shown in figure 10). For $\mathscr{R} = 100$, there are enduring fingers having no lateral motion. For $\mathscr{R} = 200$, fingers are merging, while for $\mathscr{R} = 500$ and 1000, there are mergers and spatially localized

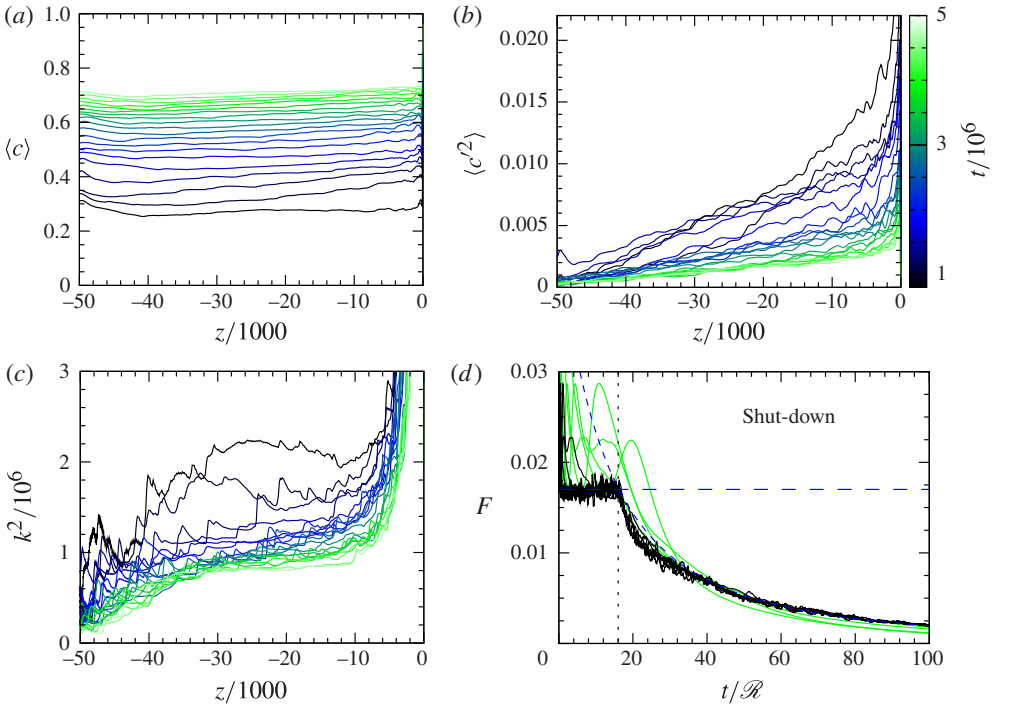

FIGURE 11. (Colour online) Solutions in the shut-down regime for $\mathscr{R} = 5 \times 10^4$: horizontally averaged (*a*) concentration, (*b*) mean-square fluctuations and (*c*) wavenumber for times between $t = 8 \times 10^5$ (darker/bluer curves) and 5×10^6 (paler/greener curves). (*d*) The dissolution flux for the same Rayleigh numbers of figure 9 against time rescaled by $\mathscr{R}$. The short-dashed line is the constant-flux regime value (3.3). The long-dashed curve is the phenomenological prediction for the shut-down regime (4.15). The curves for $\mathscr{R} = 100$ to $\mathscr{R} = 1000$ are pale/green to indicate that these do not reach the constant-flux regime and thus the latter prediction may not apply (although it is seen to be a reasonable approximation).

initiations of protoplumes. Both mergers and reinitiations become less frequent as the layer saturates.

For $\mathscr{R} \gtrsim 2000$, when the regime before transition was constant flux, reinitiations of protoplumes on the diffusive boundary layer below $z = 0$ remain the prominent dynamical feature. However, their frequency is reduced (figures 6*c* and 10*e*,*f*) as the driving density difference reduces. Mergers and coarsening continue, although the plume width grows more gradually than the $\sqrt{t}$ behaviour earlier (our simulation length was insufficient to determine a new scaling; further details are given by Hewitt *et al.* (2013)). Structurally, the downwelling primary plumes transition to a vertical columnar exchange flow (figure 4*b*) reminiscent of the equivalent thermal problem (Hewitt *et al.* 2012, 2013), although it is not simply a quasi-statically adjusting form of the latter as the layer saturates. (The sinusoidal component of the profile clearly depends on $z/\mathscr{R}$ as seen in figure 4*b*.)

During this regime, the horizontally averaged concentration profile consists of a progressively expanding upper diffusive boundary layer with an almost vertically well-mixed bulk beneath (figure 11*a*). Exploiting this observation, the gradually decaying flux can be well described by a simple box-model (Hewitt *et al.* 2013; Slim *et al.*

2013). We briefly revisit the analysis in § 4, to put it in the context of the upscaled equations and to modify the initial condition to coincide with the end of the constant-flux regime.

4. A partial derivation of upscaled equations

A key aim of our study is to derive upscaled equations that capture the fine-scale physics on a scale achievable in reservoir simulations. As described in §§ 3.5 and 3.7, the horizontally averaged concentration profile has simple, elegant forms in the constant-flux and shut-down regimes, thus we look for governing equations for horizontally averaged quantities.

4.1. *Moment equations*

First we consider the dynamics in the bulk, below the diffusive boundary layer beneath $z = 0$. We reduce the flow equation (2.8*a*,*b*) using $\partial_x[\boldsymbol{\nabla}\times(2.8a)] - \partial_z(2.8b)$ to

$$\frac{\partial^2 w}{\partial x^2} + \frac{\partial^2 w}{\partial z^2} = -\frac{\partial^2 c}{\partial x^2}. \tag{4.1}$$

The plumes are slender, so we neglect vertical derivatives over horizontal. Integrating in x, we obtain

$$w = -c', \tag{4.2}$$

where we have invoked periodicity and taken $\langle w\rangle = 0$ by incompressibility. Physically, this states that the vertical velocity is directly set by the local concentration anomaly. The approximation is good (figure 4) except where there is an upwelling of pure fluid between pioneer plumes. This result also allows us to set the downward advective flux of solute as

$$f(z,t) = -\langle wc\rangle = \langle c'^2\rangle, \tag{4.3}$$

which is the only form of vertical solute transport under the slenderness approximation.

Horizontally averaging the advection–diffusion equation for solute transport (2.8*c*), ignoring vertical diffusion over horizontal and using (4.3), we obtain

$$\frac{\partial\langle c\rangle}{\partial t} = \frac{\partial\langle c'^2\rangle}{\partial z}. \tag{4.4}$$

Physically, this is simply a conservation law for solute. Note that applying (4.2) is adequate everywhere because where the approximation is poor $c = 0$.

A closure expression for $\langle c'^2\rangle$ is not apparent, so we turn to the next moment. Multiplying (2.8*c*) by c and proceeding as above, we obtain

$$\frac{\partial\langle c'^2\rangle}{\partial t} - 2\langle c'^2\rangle\frac{\partial\langle c\rangle}{\partial z} - \frac{\partial\langle c'^3\rangle}{\partial z} = -2\langle(\partial c'/\partial x)^2\rangle = -2k^2\langle c'^2\rangle. \tag{4.5}$$

This introduces two new moments, $\langle c'^3\rangle$ and $\langle(\partial c'/\partial x)^2\rangle$. The third moment $\langle c'^3\rangle$ is generally small because upwellings and downwellings are nearly symmetric. It can be ignored except when pioneer plumes first enter a region. In this case, approximating individual plumes as portions of sinusoids (see appendix C), gives

$$\langle c'^3\rangle = \tfrac{1}{9}\langle c\rangle^3 - \tfrac{7}{9}\langle c\rangle\langle c'^2\rangle + \tfrac{10}{9}\langle c'^2\rangle^2/\langle c\rangle \quad \text{for } \langle c'^2\rangle \geqslant \langle c\rangle^2/2 \tag{4.6}$$

with good accuracy. The $\langle(\partial c'/\partial x)^2\rangle$ term can be interpreted as the local scalar dissipation rate of turbulence (for example, Hanjalic 2002; see also Hidalgo *et al.* 2012). However, we find it more meaningful to interpret it as indicative of the plume width ω through $\omega = \pi/k$ with k the wavenumber as defined in (2.21) and as indicated in (4.5).

An interpretation of (4.5) is possible through the representation (4.3): the downward advective flux f is eroded through conversion to a horizontal diffusive flux (the right-hand side of the equation) and augmented by the introduction of denser material from above and lighter from below intensifying the plumes (the term proportional to $\partial\langle c\rangle/\partial z$).

Obviously the behaviour of the plume width must be understood before this model can be predictive. This will likely take the form of a phenomenological description of the merging process and the complex interplay between upwellings and downwelling plumes. I have been unable to find a satisfactory universal expression or governing equation and leave this for future work. In §§ 4.3 and 4.4, we find solutions for the constant-flux and shut-down regimes making certain empirical assumptions. In appendix D, we also show that the model can predict the flux in the companion thermal problem given the $\mathscr{R}$-dependence of k.

These equations were also presented by Wooding (1969) for miscible Rayleigh–Taylor flow in a porous medium, with assumptions that $\langle c'^3\rangle = 0$ everywhere and $k^2 t$ is a constant.

4.2. *Boundary conditions*

Before we turn to solutions of these governing equations, we still require boundary conditions. The intention is to shrink the diffusive boundary layer beneath $z = 0$ to zero thickness and impose an effective boundary condition that describes the conversion of vertical diffusive transport into the system into vertical advective transport into the bulk.

At the top of the bulk, $z = 0^-$, we have

$$F = f = \langle c'^2\rangle \quad \text{at } z = 0^-. \tag{4.7}$$

We now look for a phenomenological description of the dissolution flux F, linking it to the horizontally averaged concentration $\langle c\rangle|_{z=0^-}$ just below the boundary layer. From Fick's law, we have

$$F(t) = \frac{1 - \langle c\rangle|_{z=0^-}}{\delta}, \tag{4.8}$$

where δ is an effective boundary-layer thickness. We now assume that the boundary layer is marginally stable (Howard 1964)

$$(1 - \langle c\rangle|_{z=0^-})\,\delta = \mathscr{R}_c, \tag{4.9}$$

where the left-hand side is an effective Rayleigh number for the boundary layer and $\mathscr{R}_c$ is a critical Rayleigh number, assumed constant. Combining these, we have

$$F = \langle c'^2\rangle = \frac{(1 - \langle c\rangle)^2}{\mathscr{R}_c} \quad \text{at } z = 0^-. \tag{4.10}$$

A reasonable approximation for $\mathscr{R}_c$ is

$$\mathscr{R}_c \approx 31.5, \tag{4.11}$$

based on the values of F and c_0 in the constant-flux regime.

At the bottom of the layer, we assume the advective flux is zero and so

$$f = \langle c'^2 \rangle = 0 \quad \text{at } z = -\mathscr{R}. \tag{4.12}$$

This is a reasonable approximation (figures 8*b*i and 11*b*), except immediately after plumes reach the bottom. At this time, the spreading gravity currents violate the slenderness approximation and (4.2) fails.

4.3. *The constant-flux regime: a similarity solution*

We first look for a similarity solution for the constant flux regime. We set $\zeta = z/t$ and $\kappa^2 = k^2 t$ in (4.4)–(4.12), with $\kappa^2(\zeta)$ taking the functional form shown in figure 8(*c*ii). Solving the resulting ordinary differential equation in ζ numerically using a shooting method, we obtain the solutions shown in figure 8(*a*ii,*b*ii), in reasonable agreement with the simulation data.

4.4. *The shut-down regime: rederiving the box model*

For the shut-down regime, we assume that $\langle c \rangle$ is uniform in z at leading order. Then integrating (4.5) from $z = -\mathscr{R}$ to $z = 0^-$, we obtain

$$\mathscr{R}\frac{\mathrm{d}\langle c \rangle}{\mathrm{d}t} = \frac{(1 - \langle c \rangle)^2}{\mathscr{R}_c}, \tag{4.13}$$

with solution

$$\langle c \rangle = \frac{(1 - c_0)t' + c_0\mathscr{R}_c}{(1 - c_0)t' + \mathscr{R}_c}, \tag{4.14}$$

where $t' = t/\mathscr{R} - 16$ and we have taken the initial condition $\langle c \rangle = c_0$ at $t' = 0$. This implies

$$F = \frac{\mathscr{R}_c(1 - c_0)^2}{\left[(1 - c_0)t' + \mathscr{R}_c\right]^2}. \tag{4.15}$$

This solution is a good fit across all $\mathscr{R}$ (figure 11*d*), albeit with a noticeable overestimate soon after transition to the shut-down regime when the bulk is not fully well-mixed.

5. The partially permeable upper boundary

We now turn to the partially permeable upper boundary scenario, where fluid from the convecting layer can be exchanged with saturated fluid in an overlying layer. We examine relative permeabilities in the upper layer $\mathscr{K} = 0.2$ and 0.6. In addition to being of practical interest in CO_2 storage, this case also provides some insight into the mechanism controlling plume width.

The qualitative behaviour is very similar to the impermeable case, with almost identical regimes and characteristics. The key difference is that convection is more intense, with higher fluxes and greater concentrations in fingers and plumes. Transitions also occur sooner. Plots of the temporal evolution on a slice just beneath the upper boundary are shown in figure 12 and the dissolution flux, horizontally averaged profiles and wavenumbers are shown in figure 13. We focus on times starting with the transition to the constant-flux regime.

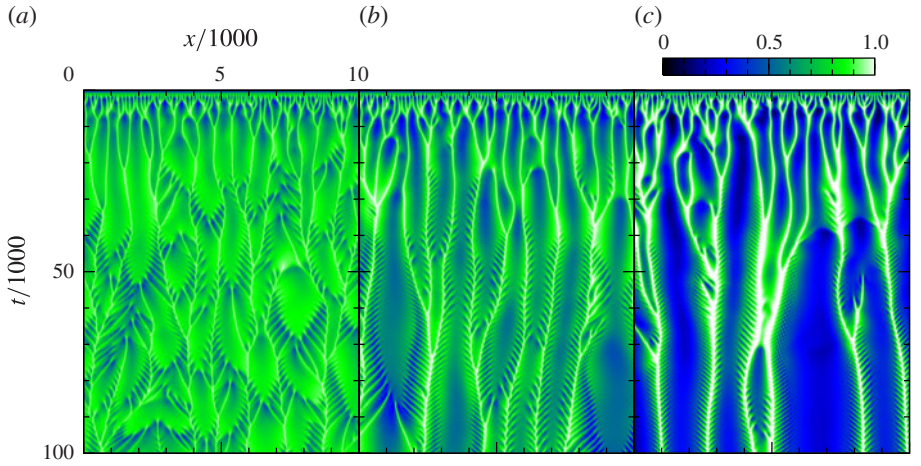

FIGURE 12. (Colour online) Partially permeable upper boundary scenario: evolution of the concentration profile on $z=-20$ in time for $\mathscr{R}=5\times10^4$ and (*a*) $\mathscr{K}=0$ (impermeable), (*b*) $\mathscr{K}=0.2$ and (*c*) $\mathscr{K}=0.6$.

Once the primary plumes are sufficiently widely spaced in the merging regime, reinitiation of protoplumes again begins. Now significant differences appear from the impermeable case. Specifically, the nature of the boundary layer below $z=0$ and the reinitiations differ substantially, and increasingly so as $\mathscr{K}$ increases (figure 12). First, the downwelling primary plumes are much broader and higher concentration, and appreciably fresher fluid exists close to the boundary. This sharpens the concentration gradient and ultimately leads to higher fluxes. Second, the protoplume pulses change markedly. For $\mathscr{K}=0.2$, protoplumes are reinitiated near the primary plume for considerable time before the pulse expands towards the stagnation point and resets the cascade (figure 12*b*). For $\mathscr{K}=0.6$, protoplumes are only reinitiated near the primary plume and do not expand to form a pulse (figure 12*c*). Thus, it is no longer entirely clear that the Howard (1964) paradigm of marginal stability of the diffusive boundary layer beneath $z=0$ applies. Beneath the boundary layer, the bulk flow is qualitatively identical. Plumes are longer and higher concentration, but evolve similarly.

Unlike the impermeable case, the flux is not immediately constant once reinitiations occur everywhere. Instead, there is a prelude of a second flux-growth regime whose origin is unclear.

In the constant-flux regime, fluxes are significantly higher: $F=0.025$ for $\mathscr{K}=0.2$ and $F=0.044$ for $\mathscr{K}=0.6$ (empirical values). However, we see remarkable agreement between the wavenumbers in the bulk (figure 13*c*). This suggests that the plume width is primarily bulk-controlled rather than boundary-layer-controlled, consistent with merging occurring via slip-streaming and commencing near the tips.

As in the impermeable case, once information about the finite thickness of the layer has reached the upper boundary, the flow transitions to a shut-down regime that retains the dynamics of the previous regime. If this last regime was constant flux, then the horizontally averaged concentration profile is again a diffusive boundary layer with an essentially uniform concentration beneath, although concentrations are higher than in the impermeable case. Surprisingly, the flux overlaps to within stochastic noise (figure 13*d*). This result is particularly intriguing because the flux depends on both the boundary-layer and bulk structures.

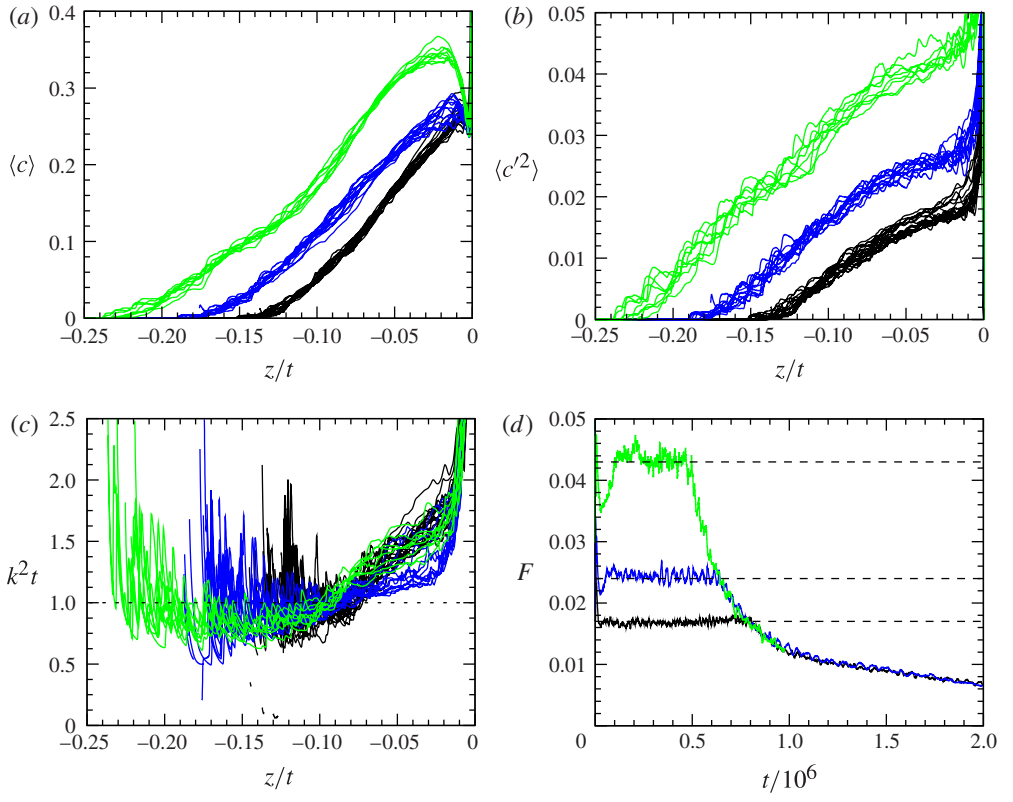

FIGURE 13. (Colour online) Partially permeable upper boundary scenario for $\mathscr{R} = 5 \times 10^4$ and $\mathscr{K} = 0$ (black curves), $\mathscr{K} = 0.2$ (dark/blue curves) and $\mathscr{K} = 0.6$ (pale/green curves). Horizontally averaged (*a*) concentration, (*b*) fluctuations and (*c*) wavenumbers for the pre-impact constant-flux regime in the similarity variable z/t. (*d*) The dissolution flux. Dashed lines at $F = 0.017$, 0.025 and 0.044 approximate the fluxes in the constant-flux regimes.

6. Summary

We have presented a simulation study of dissolution-driven convection in a two-dimensional porous medium from first contact through to high concentration for $\mathscr{R}$ from 100 to 5×10^4. We have expanded on the temporal regime diagram proposed experimentally for an impermeable upper boundary, confirming and augmenting details of the early, $\mathscr{R}$-independent regimes: pure diffusion, linear growth where fingers initiate and grow quasi-exponentially, flux growth where macroscopic fingers strip excess interfacial material and the flux increases, and merging where fingers interact and zip together over several generations to form downwelling plumes. Transition times between these depend sensitively on the initial perturbation; the structural details and evolution generally less so. Once the gap between plumes is sufficient, protoplumes are reinitiated on the horizontal boundary layer and are swept into the main plumes. The start of this process is spatially heterogeneous, but once it occurs everywhere, the universal (independent of both the initial perturbation and $\mathscr{R}$) constant-flux regime begins. We have thus shown how observations at very high $\mathscr{R}$ (Neufeld *et al.* 2010; Pau *et al.* 2010; Backhaus *et al.* 2011; Lindeberg & Wessel-Berg 2011; Hidalgo *et al.* 2012) fit into the regime delineation. In agreement

with the previous numerical work, but in contradiction with the conclusions based on experiments, we find that the flux value is independent of the Rayleigh number. This regime has a surprisingly simple solution structure: the horizontally averaged concentration evolves as a self-similar wedge and the plume width increases as $\sqrt{t}$. Information that the bottom boundary has been reached takes time to propagate upwards, and does so as an upwardly propagating wedge that overrides the self-similar wedge. Once this hits the upper boundary, the regime ends and the layer begins to saturate.

We have also studied a partially permeable upper boundary. This has use as its own problem, but also gives insight into the dominant physics because the horizontal boundary-layer structure is significantly altered from the impermeable case, but key quantities of the bulk are unchanged. Specifically, in the constant-flux regime, plume widths are quantitatively very similar, suggesting that they are bulk-controlled. In the shut-down regime, the agreement between the dissolution fluxes is remarkable. This is intriguing because the value depends on the horizontal boundary-layer structure, and suggests that understanding its origin may provide important information on physical mechanisms.

We have derived a partially complete system of upscaled equations describing horizontally averaged quantities in the constant-flux and shut-down regimes. An evolution equation for the plume widths is missing. Any such description must:

(a) presumably capture the merging process;
(b) capture a diffusive scaling in time in the constant-flux regime, with broadening from the roots to the tips;
(c) capture a subdiffusive scaling in time in the shut-down regime;
(d) be primarily bulk-controlled; and
(e) predict $k \approx 0.48/\mathscr{R}^{-3/5}$ for steady-state thermal boundary conditions in the long-time limit (see appendix D).

We have been unable to find a reasonable approximation, and leave this for future work. In lieu of a universal description, we have used appropriate assumptions in each regime and obtained reasonably good agreement between the simulated results and predictions from the equations.

6.1. *Implications for CO_2 storage in saline formations*

Finally, we return to the motivation of describing CO_2 dissolution during storage in saline formations. With present reservoir simulators, it is prohibitively expensive to use the fine grid scales required to capture the dissolution flux accurately across an entire reservoir (Lindeberg & Bergmo 2003; Riaz *et al.* 2006; Lindeberg & Wessel-Berg 2011).

For gravity-current models of evolution, a dissolution flux rate has been imposed as a boundary condition on the base of the gravity current (Gasda, Nordbotten & Celia 2011; Lindeberg & Wessel-Berg 2011; MacMinn, Szulczewski & Juanes 2011; MacMinn *et al.* 2012). From our study, we suggest that an appropriate parameterization is

$$F = \begin{cases} 1/\sqrt{\pi t} & 0 < t < 1100, \\ 0.017 & 1100 < t < 16\mathscr{R}, \\ \dfrac{16.8}{\left[0.73(t/\mathscr{R} - 16) + 31.5\right]^2} & t > 16\mathscr{R}, \end{cases} \tag{6.1}$$

rescaled according to (2.9), for a homogeneous, isotropic reservoir. Here we have approximated the perturbation-dependent regimes by the first two expressions. It is of course still necessary to understand the robustness of the estimates in three dimensions and with heterogeneities and anisotropies. The latter are known to alter the flux significantly (Cheng, Bestehorn & Firoozabadi 2012).

A flux parameterization does not readily extend to more complex scenarios with effects such as an evolving but laterally finite source or a variable background flow. In commercial simulators, a more useful alternative may be to model the evolution of aqueous CO_2 beneath the separate-phase region. This would then allow automatic capture of the evolving flux. The upscaled equations (4.4)–(4.12) are a first step towards such a model.

Supplementary movies

Supplementary movies are available at http://dx.doi.org/10.1017/jfm.2013.673.

Appendix A. Numerical scheme

We solve the governing equations numerically, introducing a streamfunction ψ such that $(u, w) = (-\partial\psi/\partial z, \partial\psi/\partial x)$. Then (2.8*a*) is satisfied automatically while $\boldsymbol{\nabla}\times$ (2.8*b*) reduces to

$$\nabla^2\psi = -\frac{\partial c}{\partial x}. \tag{A 1}$$

A.1. *Spectral scheme*

For the impermeable case, we use a spectral method in space, decomposing as Fourier modes in x and Chebyshev in z (Canuto, Hussaini & Quarteroni 2007). We work with spectral coefficients for all linear terms and physical collocation point values for the nonlinear advection term (converting via the discrete Fourier and cosine transforms provided by the FFTW package). We integrate (2.8*c*) in time using a third-order Runge–Kutta scheme for the advection term and Crank–Nicolson for the diffusion term (Canuto *et al.* 2007, §D.4). To ensure that the matrix equations arising from Poisson's equation (A 1) and the Crank–Nicolson implementation for (2.8*c*) are well-conditioned and can be solved efficiently, we use a recursion relation for second derivatives (Canuto *et al.* 2007, §4.1.2).

A.2. *Compact finite-difference scheme*

For $\mathscr{K} = 0.6$, the vertical resolution and small time steps needed for accurate results are prohibitively expensive in the spectral scheme. Instead, we use a Fourier decomposition in x and a compact finite-difference scheme in z for the partially permeable scenario.

First, we reduce the interfacial conditions and the governing equations in the overlying layer to a boundary condition. The governing equations in the upper layer also reduce to (A 1) on introducing a streamfunction, with the right-hand side becoming zero. Fourier decomposing in x and imposing decay as $z\to\infty$, the solution is found to be

$$\psi = \psi(z=0, t)\mathrm{e}^{-|m|z+\mathrm{i}mx} \quad \text{in } z>0 \tag{A 2}$$

for wavenumber m. Continuity of pressure across the boundary then implies

$$\left.\frac{\partial \psi}{\partial z}\right|_{z=0^-} = \frac{1}{\mathscr{K}} \left.\frac{\partial \psi}{\partial z}\right|_{z=0^+} \tag{A 3}$$

and, hence,

$$|m|\psi + \mathscr{K}\frac{\partial \psi}{\partial z} = 0 \quad \text{on } z = 0, \tag{A 4}$$

for Fourier mode $m \neq 0$. For $m = 0$, $\psi = 0$ on $z = 0$.

In the convecting layer, we use a stretched coordinate system in z that focuses grid points near the upper boundary. To approximate (A 1) and calculate the horizontal velocity u, we use a compact fourth-order Padé scheme together with consistent third-order boundary conditions (Carpenter, Gottlieb & Abarbanel 1993). To approximate the spatial derivatives in the concentration (2.8*c*), we use an explicit sixth-order scheme (Fornberg 1988) for the diffusive terms and the compact fourth-order scheme for vertical advection. We evolve in time using third-order Adams–Bashforth for the advective terms and Crank–Nicolson for the diffusive (see, for example, Boyd 2001, p. 229).

A.3. *Resolution*

The numerical scheme must resolve all potentially unstable waves in x. Stability analysis implies a shortest wavelength of ~ 60 (Slim & Ramakrishnan 2010). Thus, we take $8192 = 2^{13}$ Fourier modes to yield a grid spacing of approximately 12 in x. In z, we must resolve the dynamics in the horizontal boundary layer adjacent to the upper boundary. This layer is thinnest at initiation when $t = 1$ (see below), thus we need at least $1.5\sqrt{\mathscr{R}}$ Chebyshev modes (Boyd 2001, p. 59). We take 33 polynomials in z for $\mathscr{R} = 100$; 65 for $\mathscr{R} = 200$ and 500; 129 for $\mathscr{R} = 1000$ and 2000; 257 for $\mathscr{R} = 5000$ and 10 000; and 513 for $\mathscr{R} = 20\,000$ and 50 000. Results were also verified by convergence tests. For the permeable upper boundary, we take resolutions stretching from 0.2 near $z = 0$ to 20 near $z = -\mathscr{R}$.

For the impermeable upper boundary, we take a time step $\Delta t = 1$ for times up to 1000 and $\Delta t = 10$ thereafter, ensuring the CFL condition is always satisfied. For the partially permeable upper boundary, we need smaller values because higher flow speeds are attained. In either case, we find that the spatial resolution is the accuracy-limiting component (decreasing Δt does not further reduce the error whereas increasing the number of Fourier modes and Chebyshev modes/vertical grid points does).

Appendix B. Plume widths and wavenumbers

Why does (2.21) give the plume width rather than the inter-plume spacing? Consider two related, simple functions

$$c = A \sin kx \tag{B 1}$$

and

$$c = \begin{cases} A \sin kx & \text{for } 2\pi Mj/k \leqslant x \leqslant 2\pi Mj/k + \pi/k, \\ 0 & \text{otherwise,} \end{cases} \tag{B 2}$$

for j any integer and M a given positive integer. In the first, the wavelength is $2\pi/k$ and the plume width is π/k. In the second, the wavelength is $2\pi M/k$ while the width is π/k. Expression (2.21) is consistent with the widths.

Appendix C. Approximating the third moment $\langle c'^3\rangle$

The pioneer plumes can be reasonably approximated by portions of sinusoids. Setting

$$c = \begin{cases} \frac{1}{2}A(1+\cos kx) & \text{for } 2\pi Mj/k - \pi/k \leqslant x \leqslant 2\pi Mj/k + \pi/k, \\ 0 & \text{otherwise,} \end{cases} \tag{C 1}$$

and calculating the first three moments, we find that $\langle c^3\rangle = (10/9)\langle c^2\rangle^2/\langle c\rangle$. This approximation is permissible for $\langle c'^2\rangle \geqslant \langle c\rangle^2/2$. Thus, we obtain the expression (4.6).

Note that ignoring the $\langle c'^3\rangle$ term entirely results in a need for shocks. For example, in pioneer plume territory, solutions are found to curl over unphysically, which would suggest replacing the entire region with a shock (the equations are hyperbolic, provided k^2 does not introduce a first-order term). This is a substantial approximation and, more significantly, it is not clear how to correctly introduce the shock because the 'true' conservation form of (4.5) is unknown (see, for example, LeVeque 2002).

Appendix D. Upscaled model predictions for thermal convection

Further verification of the model (4.4)–(4.12) is possible by comparison with the steady-state thermal problem. In steady state, equation (4.4) implies $\langle c'^2\rangle$ is constant and (4.5) implies $\partial\langle c\rangle/\partial z = k^2$. Taking k^2 constant and replacing (4.12) with $F = \langle c'^2\rangle = \langle c\rangle^2/\mathscr{R}_c$ on $z = -\mathscr{R}$, we obtain

$$F = (1 - k^2\mathscr{R})^2/(4\mathscr{R}_c). \tag{D 1}$$

We obtain a flux approximation within 10 % of the simulated data of Hewitt *et al.* (2012), using their observed value for the wavenumber $k(\mathscr{R}) \approx 0.48/\mathscr{R}^{-3/5}$.

REFERENCES

BACKHAUS, S., TURITSYN, K. & ECKE, R. E. 2011 Convective instability and mass transport of diffusion layers in a Hele-Shaw geometry. *Phys. Rev. Lett.* **106** (10), 104501.

BARENBLATT, G. I. 1996 *Scaling, Self-similarity and Intermediate Asymptotics*. Cambridge University Press.

BOYD, J. P. 2001 *Chebyshev and Fourier Spectral Methods*. Springer.

BUSSE, F. H. & JOSEPH, D. D. 1972 Bounds for heat transport in a porous layer. *J. Fluid Mech.* **54**, 521–543.

CANUTO, C., HUSSAINI, M. Y. & QUARTERONI, A. 2007 *Spectral Methods: Fundamentals in Single Domains*. Springer.

CARPENTER, M. H., GOTTLIEB, D. & ABARBANEL, S. 1993 The stability of numerical boundary treatments for compact high-order finite-difference schemes. *J. Comput. Phys.* **108**, 272–295.

CHANDRASEKHAR, S. 1961 *Hydrodynamic and Hydromagnetic Stability*. Dover.

CHENG, P., BESTEHORN, M. & FIROOZABADI, A. 2012 Effect of permeability anisotropy on buoyancy-driven flow for CO_2 sequestration in saline aquifers. *Water Resour. Res.* **48** (9), W09539.

DOERING, C. R. & CONSTANTIN, P. 1998 Bounds for heat transport in a porous layer. *J. Fluid Mech.* **376**, 263–296.

ELDER, J. W. 1968 The unstable thermal interface. *J. Fluid Mech.* **32** (1), 69–96.

ELENIUS, M. T. & JOHANNSEN, K. 2012 On the time scales of nonlinear instability in miscible displacement porous media flow. *Comput. Geosci.* **16** (4), 901–911.

ELENIUS, M. T., NORDBOTTEN, J. M. & KALISCH, H. 2012 Effects of a capillary transition zone on the stability of a diffusive boundary layer. *IMA J. Appl. Maths* **77** (6), 771–787.

ENNIS-KING, J. & PATERSON, L. 2005 Role of convective mixing in the long-term storage of carbon dioxide in deep saline formations. *SPE J.* **10** (3), 349–356.

ENNIS-KING, J., PRESTON, I. & PATERSON, L. 2005 Onset of convection in anisotropic porous media subject to a rapid change in boundary conditions. *Phys. Fluids* **17**, 084107.

FORNBERG, B. 1988 Generation of finite difference formulas on arbitrarily spaced grids. *Math. Comput.* **51** (184), 699–706.

FOWLER, A. C. 1997 *Mathematical Models in the Applied Sciences*. Cambridge University Press.

GASDA, S. E., NORDBOTTEN, J. M. & CELIA, M. A. 2011 Vertically averaged approaches for CO_2 migration with solubility trapping. *Water Resour. Res.* **47** (5), W05528.

GRAHAM, M. D. & STEEN, P. H. 1994 Plume formation and resonant bifurcations in porous-media convection. *J. Fluid Mech.* **272** (1), 67–90.

HANJALIC, K 2002 One-point closure models for buoyancy-driven turbulent flows. *Annu. Rev. Fluid Mech.* **34** (1), 321–347.

HASSANZADEH, H., POOLADI-DARVISH, M. & KEITH, D. W. 2007 Scaling behaviour of convective mixing, with application to geological storage of CO_2. *AIChE J.* **53** (5), 1121–1131.

HEWITT, D. R., NEUFELD, J. A. & LISTER, J. R. 2012 Ultimate regime of high Rayleigh number convection in a porous medium. *Phys. Rev. Lett.* **108** (22), 224503.

HEWITT, D. R., NEUFELD, J. A. & LISTER, J. R. 2013 Convective shutdown in a porous medium at high Rayleigh number. *J. Fluid Mech.* **719**, 551–586.

HIDALGO, J. J., FE, J., CUETO-FELGUEROSO, L. & JUANES, R. 2012 Scaling of convective mixing in porous media. *Phys. Rev. Lett.* **109** (26), 264503.

HORTON, C. W. & ROGERS, F. T. 1945 Convection currents in a porous medium. *J. Appl. Phys.* **16**, 367–370.

HOWARD, L. N. 1964 Convection at high Rayleigh numbers. In *Applied Mechanics, Proceedings of 11th Congress of Applied Mathematics* (ed. H. Görtler), pp. 1109–1115.

KIM, M. C. & CHOI, C. K. 2012 Linear stability analysis on the onset of buoyancy-driven convection in liquid-saturated porous medium. *Phys. Fluids* **24**, 044102.

KNEAFSEY, T. J. & PRUESS, K. 2011 Laboratory experiments and numerical simulation studies of convectively enhanced carbon dioxide dissolution. *Energy Proc.* **4**, 5114–5121.

LAPWOOD, E. R. 1948 Convection of a fluid in a porous medium. *Proc. Camb. Phil. Soc.* **44**, 508–521.

LEVEQUE, R. J. 2002 *Finite Volume Methods for Hyperbolic Problems*. Cambridge University Press.

LINDEBERG, E. & BERGMO, P. 2003 The long-term fate of CO_2 injected into an aquifer. *Greenh. Gas Control Tech.* **1**, 489–494.

LINDEBERG, E. & WESSEL-BERG, D. 1997 Vertical convection in an aquifer column under a gas cap of CO_2. *Energy Convers. Manage.* **38**, S229–S234.

LINDEBERG, E. & WESSEL-BERG, D. 2011 Upscaling studies of diffusion induced convection in homogeneous and heterogeneous aquifers. *Energy Proc.* **4**, 3927–3934.

MACMINN, C. W., NEUFELD, J. A., HESSE, M. A. & HUPPERT, H. E. 2012 Spreading and convective dissolution of carbon dioxide in vertically confined, horizontal aquifers. *Water Resour. Res.* **48** (11), W11516.

MACMINN, C. W., SZULCZEWSKI, M. L. & JUANES, R. 2011 CO_2 migration in saline aquifers. Part 2. Capillary and solubility trapping. *J. Fluid Mech.* **688**, 321–351.

2005 In *IPCC Special Report on Carbon Dioxide Capture and Storage* (ed. B. Metz, O. Davidson, H. C. de Coninck, M. Loos & L.A. Meyer), Cambridge University Press.

NEUFELD, J. A., HESSE, M. A., RIAZ, A., HALLWORTH, M. A., TCHELEPI, H. A. & HUPPERT, H. E. 2010 Convective dissolution of carbon dioxide in saline aquifers. *Geophys. Res. Lett.* **37**, L22404.

NIELD, D. A. & BEJAN, A. 2006 *Convection in Porous Media*. Springer.

OTERO, J., DONTCHEVA, L. A., JOHNSTON, H., WORTHING, R. A., KURGANOV, A., PETROVA, G. & DOERING, C. R. 2004 High-Rayleigh-number convection in a fluid-saturated porous layer. *J. Fluid Mech.* **500** (1), 263–281.

PAU, G. S. H., BELL, J. B., PRUESS, K., ALMGREN, A. S., LIJEWSKI, M. J. & ZHANG, K. 2010 High-resolution simulation and characterization of density-driven flow in CO_2 storage in saline aquifers. *Adv. Water Resour.* **33** (4), 443–455.

RAPAKA, S., CHEN, S., PAWAR, R. J., STAUFFER, P. H. & ZHANG, D. 2008 Non-modal growth of perturbations in density-driven convection in porous media. *J. Fluid Mech.* **609**, 285–303.

REES, D. A. S., SELIM, A. & ENNIS-KING, J. P. 2008 The instability of unsteady boundary layers in porous media. In *Emerging Topics in Heat and Mass Transfer in Porous Media* Theory and Application of Transport in Porous Media, vol. 22, pp. 85–110. Springer.

RIAZ, A., HESSE, M., TCHELEPI, H. A. & ORR, F. M. 2006 Onset of convection in a gravitationally unstable diffusive boundary layer in porous media. *J. Fluid Mech.* **548**, 87–111.

SLIM, A. C., BANDI, M. M., MILLER, J. C. & MAHADEVAN, L. 2013 Dissolution-driven convection in a Hele-Shaw cell. *Phys. Fluids* **25**, 024101.

SLIM, A. C. & RAMAKRISHNAN, T. S. 2010 Onset and cessation of time-dependent, dissolution-driven convection in porous media. *Phys. Fluids* **22**, 124103.

TURNER, J. S. 1973 *Buoyancy Effects in Fluids*. Cambridge University Press.

WEIR, G. J., WHITE, S. P. & KISSLING, W. M. 1996 Reservoir storage and containment of greenhouse gases. *Transp. Porous Media* **23** (1), 37–60.

WOODING, RA 1969 Growth of fingers at an unstable diffusing interface in a porous medium or Hele-Shaw cell. *J. Fluid Mech.* **39** (3), 477–495.

XIE, Y., SIMMONS, C. T. & WERNER, A. D. 2011 Speed of free convective fingering in porous media. *Water Resour. Res.* **47** (11), W11501.